ORIGINAL ARTICLE

Journal Section

Legacy Recovery and Robust Augmentation Structured Design for the VEGA Launcher

D. Navarro-Tapia[1] | A. Marcos[1] | P. Simplício[1] | S. Bennani[2] | C. Roux[3]

[1]Technology for Aerospace Control (TASC) Lab., Department of Aerospace Engineering, University of Bristol, Bristol BS8 1TR, UK

[2]ESTEC, European Space Agency, Noordwijk, 2201AZ, The Netherlands

[3]AVIO, VEGA GNC Department, Colleferro, 00034, Italy

Correspondence
Diego Navarro-Tapia, Technology for AeroSpace Control (TASC) Lab., Department of Aerospace Engineering, University of Bristol, Bristol BS8 1TR, United Kingdom.
Email: diego.navarro-tapia@bristol.ac.uk

Funding information
European Space Agency, Networking/Partnering Initiative, Contract Number: 4000114460/15/NL/MH/ats; Engineering and Physical Sciences Research Council (EPSRC), Doctoral Training Partnership, Award Number: 1609551

This paper presents a systematic robust control framework based on the structured $\mathcal{H}_\infty$ approach to address the synthesis of the atmospheric ascent-flight control system of a launch vehicle. To introduce this synthesis framework, the control problem is first formulated to recover the classically-designed baseline rigid-body controller of the actual VEGA launcher VV05 mission. This legacy recovery builds the necessary background for a good understanding of the problem and increases confidence for its transfer to the Space industry. Subsequently, it is shown how to systematically augment the robustness of the design from the synthesis stage against first wind turbulence perturbations and then parametric uncertainty. The resulting controller is verified via classical stability margins and robust structured singular value analyses, and finally validated using nonlinear, time-domain simulations in a Monte Carlo campaign. It is highlighted that this robust synthesis framework allows to obtain a controller with improved robust stability and global performance and more importantly it provides a more systematic methodology for design.

KEYWORDS
VEGA launcher, robust control synthesis, structured $\mathcal{H}_\infty$, μ analysis

1 | INTRODUCTION

The atmospheric flight is the most challenging phase of a launch vehicle mission from a control point of view. The control of this stage is generally performed by a Thrust Vector Control (TVC) system, which must ensure stability to guidance commands while satisfying very demanding and tight performance requirements in the presence of external disturbances, such as wind gusts. Moreover, the control system must be robust against a wide range of parameter dispersions.

The VEGA launcher uses a classical design framework [1], which has been proved to be successful in all the VEGA missions performed so far, but several practical limitations are recognized. With the current state-of-practice design approach, the design has to be performed in several iterative phases and it is very difficult to achieve uniform stability and performance robustness throughout the entire flight. Furthermore, the control system design is

performed for nominal conditions and consequently, the verification and validation process must rely in an extensive analysis coverage after design. Unfortunately, due to the wide range of mission configurations and trajectories, the TVC control laws need to be updated and tailored for each mission.

To overcome these limitations, this article proposes the use of a more systematic control design framework based on the recently developed structured $\mathcal{H}_\infty$ approach [2, 3]. Significant contributions have been presented using the structured $\mathcal{H}_\infty$ approach in the last decade, resulting already in relevant Space flown missions [4, 5], piloted flight tests [6] and launch vehicle control design [7, 8, 9, 10].

This synthesis approach allows to perform a methodological control tuning for a specified controller structure. Therefore, the design can be tailored to the current VEGA TVC architecture. This is quite important since this framework can be used then as a benchmark to explore the room for improvement with respect to the baseline controller. Furthermore, the structured $\mathcal{H}_\infty$ offers more design capabilities than classical techniques. These improvements include: direct trade-off between robustness versus performance, reduce tuning effort and cost prior each mission flight, and the capability to directly include system uncertainties in the design.

This article continues the work in [11], where a launcher uncertainty modelling and a systematic analysis of the VEGA baseline controller was presented. As a follow-up, the aim in here is to provide a detailed understanding on how the launch vehicle control system design is formulated as a robust control framework and how this enables to augment the capabilities of the design. First, to increase confidence by Industry and facilitate the transfer of this technique, the structured $\mathcal{H}_\infty$ synthesis is used to recover the legacy behaviour of the baseline controller (which was designed using a classical design approach). Note, that this is not a simple reverse engineering of the baseline controller, rather, the recovery is performed based on analytical understanding of the launcher problem and systematic design weight tuning. The importance of this recovery is that an optimization-based approach is shown to recover exactly the baseline gains without using that information to initialise the control problem. Then, the level of complexity of the design interconnection is gradually increased incorporating more information about the system (i.e. statistical wind models and parametric uncertainties). This design augmentation further extends the synthesis capabilities of the structured $\mathcal{H}_\infty$ approach presented in references [7, 8, 9, 10] and is shown to be key in getting the best out of the control optimisation.

This article is organized as follows. Section 2 introduces the VEGA launcher model as well as the LFT formulation used to capture the expected variations in the system parameters. Then, the structured $\mathcal{H}_\infty$ control design is formulated to recover the legacy behaviour of the baseline controller in Section 3. Subsequently, in Section 4 the design framework is augmented providing the control optimisation with more information about the system. Finally, Section 5 ends with the conclusions.

2 | VEGA LAUNCHER BENCHMARK

This section describes the VEGA launch vehicle and its atmospheric phase mission configuration. First, the equations of motion are derived in detail and expressed in a state-space representation. Then, the LFT modeling and the uncertain parameters used in this work are presented. Finally, the VEGA control architecture for the atmospheric phase and the main requirements for this first phase of the VEGA mission are introduced.

2.1 | VEGA launcher and mission

VEGA launcher is the new European Small Launch Vehicle developed under the responsibility of the European Space Agency (ESA) and European Launch Vehicle (ELV) as prime contractor. The launcher has successfully performed thirteen launches since its maiden flight on 13^{th} February 2012. This launcher addresses the small and mini-satellites market, which covers satellites from 300 kg to 2500 kg. These satellites are used for many specific and Earth observation missions using mainly Sun Synchronous Orbits (SS0) and Low Earth Orbits (LEO).

VEGA is a single-body launcher, which follows a four-stage approach formed by three solid propellant motors (P80, Zefiro 23 and Zefiro 9) providing thrust for the first three stages; and, a bi-propellant liquid engine (LPS) on the 4^{th} stage. All stages are controlled using a TVC system. There is also a Roll and Attitude Control System (RACS) performing 3-axes control during the ballistic phase and roll rate control during the propelled phases.

2.2 | VEGA launcher model

The motion of the vehicle is described by the standard six-degree-of-freedom equations of motion, which account for the translational and rotational dynamics of the launch vehicle. The derivation of the equations of motion of a generic launch vehicle can be found in reference [12].

Due to axial symmetry of the vehicle about the roll axis, the pitch and yaw axes can be assumed uncoupled and more importantly equal. Consequently, the design and analysis can be performed in a single plane, either the pitch or the yaw axis. It should be remarked that this strategy is only valid if the roll rate is considered negligible, which is a standard assumption in launcher vehicle TVC designs and it should be noted that its effects are typically examined ad hoc [13]. In this work, the VEGA launch vehicle will be examined in the yaw plane.

The translational and rotational equations are expressed in equations 1 and 2 as the sum of forces and moments from rigid-body (F_R, M_R), flexible-body (F_F, M_F) and nozzle motion dynamics (F_N, M_N). The latter is also known as the tail-wag-dog effect in the launcher field. In addition, other contributions such as rigid damping and wind disturbances are included via the corresponding forces and moments.

$$m\ddot{z} = \Sigma F_\psi = F_R + F_F + F_N \tag{1}$$

$$\mathrm{I}_{yy}\ddot{\psi} = \Sigma M_\psi = M_R + M_F + M_N \tag{2}$$

where m is the vehicle mass, I_{yy} is the lateral moment of inertia, $\ddot{z}$ is the linear drift acceleration and $\ddot{\psi}$ the yaw attitude acceleration.

Rigid-body dynamics

The rigid-body model describes the vehicle motion due to thrust and aerodynamics. The yaw-plane rigid-body model is illustrated in Figure 1a. Using small-angle approximations, the rigid-body motion forces F_R and moments M_R in the inertial coordinate frame are given by:

$$F_R = -(T - D)\psi - N\alpha - T\beta_\psi \tag{3}$$

$$M_R = N\alpha l_{CP} - T\beta_\psi l_{CG} \tag{4}$$

where T is the gimbaled thrust force, D the aerodynamic drag force and $N\alpha$ the force gradient with respect to the angle of attack α. The latter is formed by $N = QS_{ref}C_{N\alpha}$, where Q is the dynamic pressure, S_{ref} is the launcher reference area and $C_{N\alpha}$ is the lift coefficient gradient with respect to α. The distance from the center of gravity (CG) x-coordinate x_{CG} to the aerodynamic center of pressure (CP) x-coordinate x_{CP} is given by l_{CP} while l_{CG} is the distance from CG to the nozzle pivot point (PVP). The main angles in this dynamic model are the yaw attitude angle ψ and the actuator deflection in the yaw plane β_ψ.

Note that the angle of attack α is described by a component with respect to the ground α_{ground} and a wind induced term α_w as follows:

$$\alpha = \alpha_{ground} - \alpha_w = \psi + \frac{\dot{z}}{V} - \frac{v_w}{V} \tag{5}$$

where $\alpha_{ground} = \psi + \gamma$ and $\alpha_w = \frac{v_w}{V}$, with V the vehicle velocity with respect to the ground, v_w the wind velocity and γ the drift angle defined as $\frac{\dot{z}}{V}$.

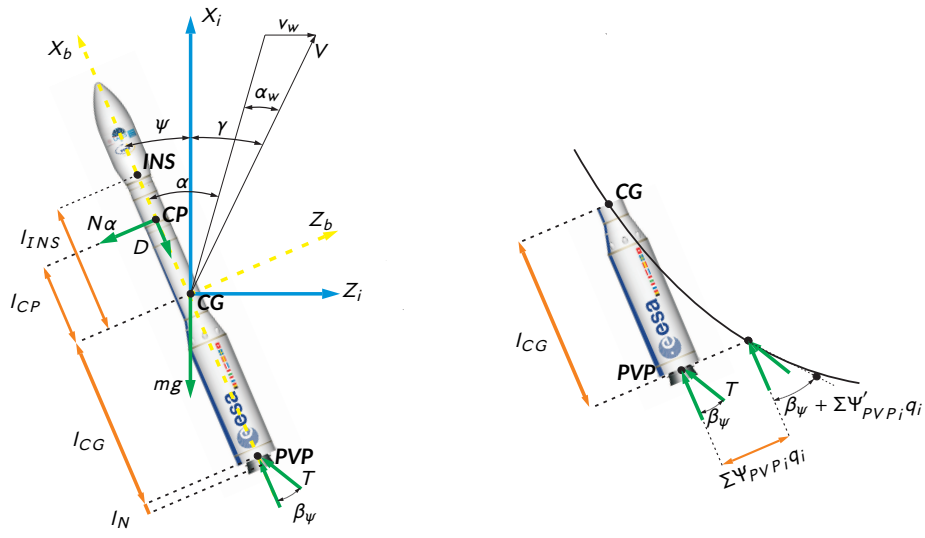

(a) Rigid-body diagram

(b) Flexible-body diagram

FIGURE 1 VEGA yaw-axis diagram

Nozzle dynamics

The motion of the gimbaled engines creates inertia forces and torques (the aforementioned tail-wag-dog effect), which must be taken into account. The lateral force F_N and moment M_N due to nozzle dynamics are given by:

$$F_N = -m_N l_N \ddot{\beta}_\psi \tag{6}$$

$$M_N = -(m_N l_N l_{CG} + \mathrm{I_N})\ddot{\beta}_\psi \tag{7}$$

where $\ddot{\beta}_\psi$ is the acceleration of the actuator in the yaw plane, m_N is the nozzle mass and l_N is the distance from the nozzle center of gravity to the PVP. The moment of inertia of the nozzle engine about the PVP is given by $\mathrm{I_N} = \mathrm{I_o} + m_N l_N^2$, where $\mathrm{I_o}$ is the moment of inertia of the nozzle engine about its center of gravity.

Flexible-body dynamics

The flexible-body model in Figure 1b represents the elastic behaviour of the launch vehicle. The flexible motion for the i^{th} bending mode is represented by the following 2^{nd} order model with a natural frequency ω_{q_i} and a low damping ratio ζ_{q_i}:

$$\ddot{q}_i + 2\zeta_{q_i}\omega_{q_i}\dot{q}_i + \omega_{q_i}^2 q_i = -T\Psi_{PVPi}\beta_\psi - (m_N l_N \Psi_{PVPi} - \mathrm{I_N}\Psi'_{PVPi})\ddot{\beta}_\psi \tag{8}$$

where q_i is the state of the i^{th} bending mode, and Ψ'_{PVPi} and Ψ_{PVPi} are the rotational and translational lengths of the i^{th} bending mode at PVP respectively.

In addition, the bending modes produce an additional lateral perturbation and create a local rotation added to the commanded gimbaled angle β_ψ. The elastic forces and moments expressed in the inertial coordinate frame are given by:

$$F_F = T \sum_{i=1}^{k} \Psi'_{PVP_i} q_i \tag{9}$$

$$M_F = -T\left(l_{CG} \sum_{i=1}^{k} \Psi'_{PVP_i} q_i + \sum_{i=1}^{k} \Psi_{PVP_i} q_i\right) \tag{10}$$

Sensors characterization

The sensed values are defined at the node location of the inertial navigation system (INS), which is typically located in the upper stage at a distance l_{INS} from CG (see Figure 1a). In addition, the influence of the flexible-body motion at the sensor location is also considered. The sensed attitude, drift and their derivatives are given by:

$$\psi_{INS} = \psi - \sum_{i=1}^{k} \Psi'_{INS_i} q_i \tag{11}$$

$$\dot{\psi}_{INS} = \dot{\psi} - \sum_{i=1}^{k} \Psi'_{INS_i} \dot{q}_i \tag{12}$$

$$z_{INS} = z - l_{INS}\psi + \sum_{i=1}^{k} \Psi_{INS_i} q_i \tag{13}$$

$$\dot{z}_{INS} = \dot{z} - l_{INS}\dot{\psi} + \sum_{i=1}^{k} \Psi_{INS_i} \dot{q}_i \tag{14}$$

where Ψ'_{INS_i} and Ψ_{INS_i} are the rotational and translational lengths of the i^{th} bending mode at INS.

State-space representation

In this article, the dynamic model is built following reference [14], where the equations of motion are expressed as a state-space representation suitable for analysis and design. All relevant dynamics are expressed using the state-space formulation shown in equation 15, where the rigid and flexible-body contributions are expressed separately.

$$\begin{aligned} \begin{bmatrix} \dot{\mathbf{x}}_\mathbf{R} \\ \dot{\mathbf{x}}_\mathbf{F} \end{bmatrix} &= \begin{bmatrix} A_R & A_{RF} \\ A_{FR} & A_F \end{bmatrix} \begin{bmatrix} \mathbf{x}_\mathbf{R} \\ \mathbf{x}_\mathbf{F} \end{bmatrix} + \begin{bmatrix} B_R \\ B_F \end{bmatrix} \mathbf{u_{LV}} \\ \mathbf{y_{LV}} &= \begin{bmatrix} C_R & C_F \end{bmatrix} \begin{bmatrix} \mathbf{x}_\mathbf{R} \\ \mathbf{x}_\mathbf{F} \end{bmatrix} + D_R\, \mathbf{u_{LV}} \end{aligned} \tag{15}$$

The launch vehicle state-space model uses four rigid-body states given by the drift z, yaw attitude angle ψ and their derivatives $\left(\mathbf{x_R} = \begin{bmatrix} z & \dot{z} & \psi & \dot{\psi} \end{bmatrix}^T\right)$; $2k$ flexible-body states accounting for k bending modes $\left(\mathbf{x_F} = \begin{bmatrix} \mathbf{q} & \dot{\mathbf{q}} \end{bmatrix}^T\right.$ with $\mathbf{q} = \begin{bmatrix} q_1 \cdots q_k \end{bmatrix}$ and $\dot{\mathbf{q}} = \left.\begin{bmatrix} \dot{q}_1 \cdots \dot{q}_k \end{bmatrix}\right)$; five outputs $\left(\mathbf{y_{LV}} = \begin{bmatrix} Q\alpha & \psi_{INS} & \dot{\psi}_{INS} & z_{INS} & \dot{z}_{INS} \end{bmatrix}^T\right)$, which include the load performance indicator $Q\alpha$ and the measurements at INS node location for the four rigid-body states; and three inputs $\left(\mathbf{u_{LV}} = \begin{bmatrix} \beta_\psi & \ddot{\beta}_\psi & v_w \end{bmatrix}^T\right)$. The matrices of the state-space model are given in equation 16.

$$
\begin{bmatrix} \dot{z} \\ \ddot{z} \\ \dot{\psi} \\ \ddot{\psi} \\ \hdashline \dot{\mathbf{q}} \\ \ddot{\mathbf{q}} \end{bmatrix} = \left[\begin{array}{cccc:cc} 0 & 1 & 0 & 0 & 0_{1\mathbf{k}} & 0_{1\mathbf{k}} \\ 0 & a_1 & a_3 & a_2 & \mathbf{a_{zq}} & 0_{1\mathbf{k}} \\ 0 & 0 & 0 & 1 & 0_{1\mathbf{k}} & 0_{1\mathbf{k}} \\ 0 & a_4 & a_6 & a_5 & \mathbf{a_{\psi q}} & 0_{1\mathbf{k}} \\ \hdashline 0_{\mathbf{k}1} & 0_{\mathbf{k}1} & 0_{\mathbf{k}1} & 0_{\mathbf{k}1} & 0_{\mathbf{kk}} & \mathbf{I_k} \\ 0_{\mathbf{k}1} & 0_{\mathbf{k}1} & 0_{\mathbf{k}1} & 0_{\mathbf{k}1} & \mathbf{a_{qq}} & \mathbf{a_{q\dot{q}}} \end{array}\right] \begin{bmatrix} z \\ \dot{z} \\ \psi \\ \dot{\psi} \\ \hdashline \mathbf{q} \\ \dot{\mathbf{q}} \end{bmatrix} + \left[\begin{array}{ccc} 0 & 0 & 0 \\ a_p & k_2 & -a_1 \\ 0 & 0 & 0 \\ k_1 & k_3 & -a_4 \\ \hdashline 0_{\mathbf{k}1} & 0_{\mathbf{k}1} & 0_{\mathbf{k}1} \\ \mathbf{a_{q\beta}} & \mathbf{a_{q\ddot{\beta}}} & 0_{\mathbf{k}1} \end{array}\right] \begin{bmatrix} \beta_\psi \\ \ddot{\beta}_\psi \\ v_w \end{bmatrix} \tag{16}
$$

$$
\begin{bmatrix} Q\alpha \\ \psi_{INS} \\ \dot{\psi}_{INS} \\ z_{INS} \\ \dot{z}_{INS} \end{bmatrix} = \left[\begin{array}{cccc:cc} 0 & Q/V & Q & 0 & 0_{1\mathbf{k}} & 0_{1\mathbf{k}} \\ 0 & 0 & 1 & 0 & -\mathbf{a_{\Psi' q}} & 0_{1\mathbf{k}} \\ 0 & 0 & 0 & 1 & 0_{1\mathbf{k}} & -\mathbf{a_{\Psi' q}} \\ 1 & 0 & -l_{INS} & 0 & \mathbf{a_{\Psi q}} & 0_{1\mathbf{k}} \\ 0 & 1 & 0 & -l_{INS} & 0_{1\mathbf{k}} & \mathbf{a_{\Psi q}} \end{array}\right] \begin{bmatrix} z \\ \dot{z} \\ \psi \\ \dot{\psi} \\ \hdashline \mathbf{q} \\ \dot{\mathbf{q}} \end{bmatrix} + \begin{bmatrix} 0 & 0 & -Q/V \\ 0 & 0 & 0 \\ 0 & 0 & 0 \\ 0 & 0 & 0 \\ 0 & 0 & 0 \end{bmatrix} \begin{bmatrix} \beta_\psi \\ \ddot{\beta}_\psi \\ v_w \end{bmatrix}
$$

where $0_{\mathbf{ij}}$ is an $i \times j$ matrix filled with zeros and $\mathbf{I_i}$ is the identity matrix of size i. The rigid-body matrix coefficients are defined in terms of physical parameters as follows:

$$
\begin{aligned}
&a_1 = \tfrac{-N}{mV}; \quad a_2 = -a_1 l_{CP}; \quad a_3 = -acc + a_1 V; \quad a_4 = \tfrac{N}{\mathrm{I_{yy}} V} l_{CP}; \quad a_5 = -a_4 l_{CP}; \quad a_6 = a_4 V; \\
&k_1 = -\tfrac{T}{\mathrm{I_{yy}}} l_{CG}; \quad k_2 = \tfrac{m_N}{m} l_N; \quad k_3 = \tfrac{1}{\mathrm{I_{yy}}}(m_N l_N l_{CG} - \mathrm{I_N}); \quad a_p = -\tfrac{T}{m}; \quad acc = \tfrac{T-D}{m};
\end{aligned} \tag{17}
$$

Similarly, the flexible-body matrix coefficients are given by:

$$
\begin{aligned}
&\mathbf{a_{zq}} = \left[a_{zq_1} \cdots a_{zq_k}\right], \text{where } a_{zq_k} = \tfrac{T}{m} \Psi'_{PVP_k}; \quad \mathbf{a_{\psi q}} = \left[a_{\psi q_1} \cdots a_{\psi q_k}\right], \text{where } a_{\psi q_k} = \tfrac{T}{\mathrm{I_{yy}}}(\Psi'_{PVP_k} l_{CG} + \Psi_{PVP_k}); \\
&\mathbf{a_{q\beta}} = \left[a_{q\beta_1} \cdots a_{q\beta_k}\right]^T, \text{where } a_{q\beta_k} = -T\Psi_{PVP_k}; \quad \mathbf{a_{q\ddot{\beta}}} = \left[a_{q\ddot{\beta}_1} \cdots a_{q\ddot{\beta}_k}\right]^T, \text{where } a_{q\ddot{\beta}_k} = \mathrm{I_N}\Psi'_{PVP_k} - m_N l_N \Psi_{PVP_k}; \\
&\mathbf{a_{qq}} = diag\left(a_{qq_1} \cdots a_{qq_k}\right), \text{where } a_{qq_k} = -\omega_{q_k}^2; \quad \mathbf{a_{q\dot{q}}} = diag\left(a_{q\dot{q}_1} \cdots a_{q\dot{q}_k}\right), \text{where } a_{q\dot{q}_k} = -2\zeta_{q_k}\omega_{q_k}; \\
&\mathbf{a_{\Psi q}} = \left[\Psi_{INS_1} \cdots \Psi_{INS_k}\right]; \quad \mathbf{a_{\Psi' q}} = \left[\Psi'_{INS_1} \cdots \Psi'_{INS_k}\right];
\end{aligned} \tag{18}
$$

Atmospheric phase evolution

For analysis and design purposes, the launch vehicle model previously presented is used to derive nominal Linear Time-Invariant (LTI) models at different operating points along the atmospheric flight. In addition, this formulation can also be used to further derive Linear Fractional Transformation (LFT) and Linear Parameter Varying (LPV) models. The extension to LFT is presented in Section 2.3, while the augmentation to LPV is not covered in this paper.

In this work, the launch vehicle model is built using the actual VEGA VV05 mission data [15]. During the first phase, the launch vehicle reaches Mach 5 and approximately 50 km of altitude (see Figure 2a). All physical flight parameters vary greatly during the atmospheric phase trajectory (i.e. note the dynamic pressure Q in Figure 2b). Recall that the dynamic pressure evolves as $Q = \frac{1}{2}\rho v^2$. It increases with the square of the velocity, but at a certain altitude it starts decreasing once the low air density ρ has a predominant effect. Finally, Figure 2c shows the time evolution of the aerodynamic instability coefficient a_6 and the control efficiency parameter k_1. These two parameters are critical in launcher design [1, 16], since they determine the main rigid-body motion dynamics through the relation $\ddot{\psi} = a_6\alpha + k_1\beta_\psi$.

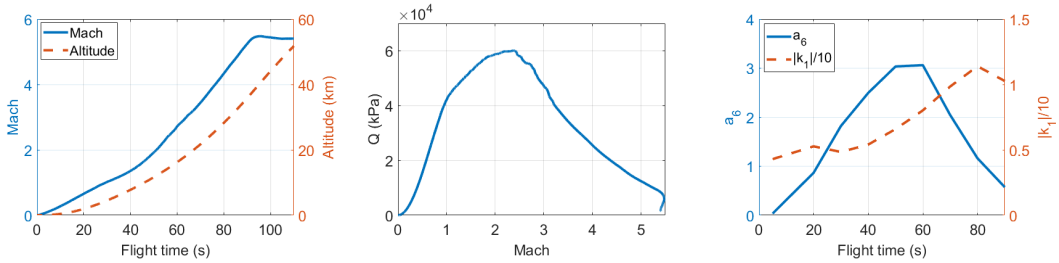

(a) Mach and altitude versus time (b) Dynamic pressure versus Mach (c) Rigid-body rotational parameters

FIGURE 2 VEGA VV05 mission parameters

To illustrate the effect of the wide dynamic variation of the mission, the frequency responses of the nominal launch vehicle model are shown in Figure 3a. Note that only the first two bending modes are modelled, which are the most relevant for design and analysis purposes. It can be seen in Figure 3a that the magnitude evolves with time presenting different characteristics throughout the atmospheric phase. This plot also shows that the frequency of each bending mode peak increases with time. This behaviour is also confirmed looking at the pole migration map shown in Figure 3b. In this case, the launch vehicle model presents eight poles, four rigid-body and four flexible-body poles accounting for the two bending modes. It should be remarked that, as typical for launcher systems in open-loop, two of the rigid-body poles are unstable (see right-hand side of Figure 3b). The main stabilisation control problem comes from the larger unstable pole, which is mainly governed by the rotational motion of the vehicle and it is approximately placed at $s = \sqrt{a_6}$. This pole highly varies with time and since a_6 is proportional to Q (see Figure 2), it reaches its maximum value around the maximum dynamic pressure region (t = 50-60 s). Besides the stabilisation issue, the control problem is also very challenging from a performance point of view because the launch vehicle encounters the highest aerodynamic loads around this region. This demands more control actuation in order to counteract the torque generated by the structural loads. With respect to the second unstable pole, which is closer to the origin, it is mainly caused by the translational motion of the vehicle and it requires less control effort to stabilise due to its slow dynamics behaviour.

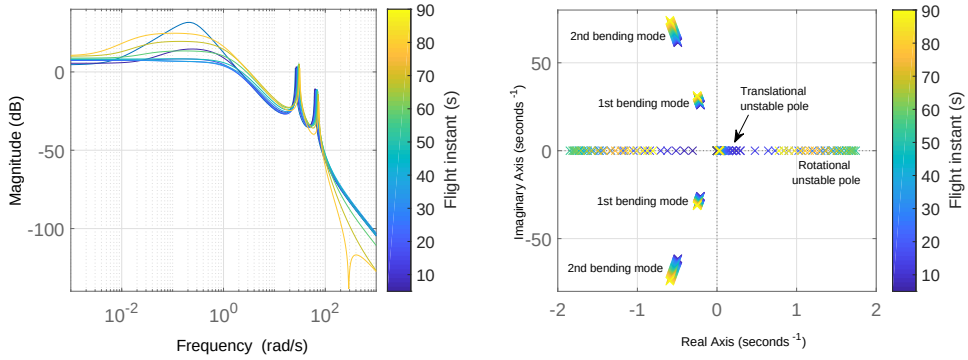

(a) Attitude frequency responses ($\psi_{INS}/\beta_\psi(j\omega)$) (b) Launch vehicle pole migration map

FIGURE 3 Launch Vehicle open-loop time-varying properties

2.3 | LFT modelling

The Linear Fractional Transformation (LFT) theory allows to consider plant uncertainties for analysis and design purposes. The LFT formulation is a suitable approach to model the known unknowns of the system and it certainly provides an additional level of insight at the design stage to provide good robustness against system uncertainties. In this section, the LFT modelling for the launcher and the actuation chain models (TVC actuator and delay) is described.

VEGA launch vehicle LFT model

The LFT model of the VEGA launcher is derived by augmenting the LTI nominal model presented in Section 2.2 with additive parametric uncertainties. This type of uncertainty is generally defined as $x = x^0 + \sigma_x \delta_x$, where x^0 represents the nominal value of parameter x, σ_x is the level of uncertainty and δ_x is a norm-bounded uncertainty flag ($||\delta_x||_\infty \leq 1$). Standard LFT modelling approaches generally define a different uncertainty flag for each variable of the model [11]. This strategy results in highly accurate LFT models but also of high complexity (in terms of number of uncertain parameters used and their repetitions).

However, for robust design and particularly for robust analysis (i.e. structured singular value, IQC), it is desirable to employ LFT models with low complexity. In that regard, the approach used in this work employs a reduced set of uncertainty flags that captures the variability of the system parameters with respect to the nominal flight while reducing the complexity of the model. Thus, the uncertainty model is re-defined as $x = x^0 + \sigma_x^{\#} \delta_{\#}$, where $\sigma_x^{\#}$ is the variability level of parameter x with respect to the flag $\delta_{\#}$. This subset of uncertainty flags are identified through a time-domain sensitivity analysis using the high-fidelity, nonlinear 6 degrees-of-freedom simulator VEGACONTROL [17]. A more detailed description of this modelling approach can be found in [18].

Table 1 shows the list of uncertain parameters. The selected parametric set is formed by 6 rigid-body scattering flags: combustion time δ_{dTc}, atmospheric density δ_ρ, and dispersions and uncertainties for the normal aerodynamic coefficient (δ_{dispCN}, δ_{uncCN}) and the center of pressure x-coordinate ($\delta_{disp X_{CP}}$ and $\delta_{unc X_{CP}}$); and 5 flexible-body scattering flags: bending frequencies δ_{ω_q} and rotations and translations at PVP and INS ($\delta_{\Psi_{PVP}}, \delta_{\Psi'_{PVP}}, \delta_{\Psi_{INS}}, \delta_{\Psi'_{INS}}$). The nominal values and uncertainty levels of each rigid-body parameter are obtained from nonlinear time-domain simulations using the VEGACONTROL simulator [18]. On the other hand, the corresponding values for the flexible-body parameters are directly extracted from the mission data used by VEGACONTROL. Note that the implementation and definition of the uncertain parameters is performed using the MATLAB Robust Control Toolbox [19].

TABLE 1 List of uncertain parameters for the VEGA launch vehicle LFT model.

Rigid-body uncertain parameters	Flexible-body uncertain parameters
$m = m^0 + \sigma_m^{dTc} \delta_{dTc}$	$\omega_{q_i} = \omega_{q_i}^0 + \sigma_{\omega_{q_i}}^{\omega_q} \delta_{\omega_q}$
$x_{CG} = x_{CG}^0 + \sigma_{X_{CG}}^{dTc} \delta_{dTc}$	$\Psi_{PVPi} = \Psi_{PVPi}^0 + \sigma_{\Psi_{PVPi}}^{\Psi_{PVP}} \delta_{\Psi_{PVP}}$
$I_{yy} = I_{yy}^0 + \sigma_{I_{yy}}^{dTc} \delta_{dTc}$	$\Psi'_{PVPi} = \Psi'^0_{PVPi} + \sigma_{\Psi'_{PVPi}}^{\Psi'_{PVP}} \delta_{\Psi'_{PVP}}$
$CN = CN^0 + \sigma_{CN}^{dispCN} \delta_{dispCN} + \sigma_{CN}^{uncCN} \delta_{uncCN}$	$\Psi_{INSi} = \Psi_{INSi}^0 + \sigma_{\Psi_{INSi}}^{\Psi_{INS}} \delta_{\Psi_{INS}}$
$x_{CP} = x_{CP}^0 + \sigma_{CN}^{dispX_{cp}} \delta_{disp X_{CP}} + \sigma_{X_{CP}}^{uncX_{CP}} \delta_{unc X_{CP}}$	$\Psi'_{INSi} = \Psi'^0_{INSi} + \sigma_{\Psi'_{INSi}}^{\Psi'_{INS}} \delta_{\Psi'_{INS}}$
$T = T^0 + \sigma_T^{dTc} \delta_{dTc}$	
$V = V^0 + \sigma_V^{dTc} \delta_{dTc}$	with $i = 1 \ldots k$
$Q = Q^0 + \sigma_Q^{dTc} \delta_{dTc} + \sigma_Q^{\rho} \delta_\rho$	
$acc = acc^0 + \sigma_{acc}^{dTc} \delta_{dTc} + \sigma_{acc}^{\rho} \delta_\rho$	

The VEGA LFT model can be represented using the so-called upper LFT interconnection shown in Figure 4. This feedback representation is described by equation 19, where $\mathcal{F}_u$ denotes the upper LFT operator, Δ_{LV} is the uncertainty matrix and $G_{LV}(s)$ defines the known part of the launch vehicle model. Note that $G_{LV}(s)$ is partitioned in four submatrices: G_{LV22} represents the nominal plant and G_{LV12}, G_{LV21} and G_{LV22} describe how the nominal plant is affected by the uncertainty matrix Δ_{LV}.

$$\mathcal{F}_u(G_{LV}(s), \Delta_{LV}) = G_{LV22} + G_{LV21}\Delta_{LV}(I - G_{LV11}\Delta_{LV})^{-1}G_{LV12} \tag{19}$$

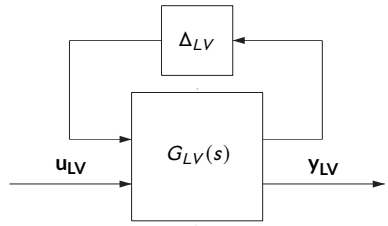

FIGURE 4 VEGA LFT model

The VEGA LFT model has dimension 95 (i.e. number of repetitions). It should be remarked that prior to the design and analysis stages, the model is simplified using LFT reduction methods and finally results in a smaller LFT dimension of 41. Also note that Δ_{LV} is defined within the uncertainty set $\mathbf{\Delta_{LV}}$ described in equation 20, where $I_\flat$ is the identity matrix of size $\flat$, and represents the number of repetitions of each uncertain parameter.

$$\begin{aligned}\mathbf{\Delta_{LV}} = \Big\{ & diag(\delta_{dTC}\mathrm{I}_{14}, \delta_\rho \mathrm{I}_3, \delta_{dispCN}\mathrm{I}_2, \delta_{uncCN}\mathrm{I}_2, \delta_{dispX_{CP}}\mathrm{I}_3, \delta_{uncX_{CP}}\mathrm{I}_3, \delta_{\omega_q}\mathrm{I}_4, \delta_{\Psi_{PVP}}\mathrm{I}_3, \delta_{\Psi'_{PVP}} I_3, \delta_{\Psi_{INS}}\mathrm{I}_2, \delta_{\Psi'_{INS}}\mathrm{I}_2); \\ & \delta_\# \in \mathbb{R}; ||\delta_\#||_\infty \leq 1 \Big\}\end{aligned} \tag{20}$$

To illustrate the effect of model perturbations on the launch vehicle model, the frequency response of the nominal VEGA attitude channel at t = 50 s (in red) and 1000 random scattered responses are shown in Figure 5a. It is shown that the LFT model defines dispersions for low frequencies (rigid-body dynamics) and also for high frequencies (flexible-body dynamics).

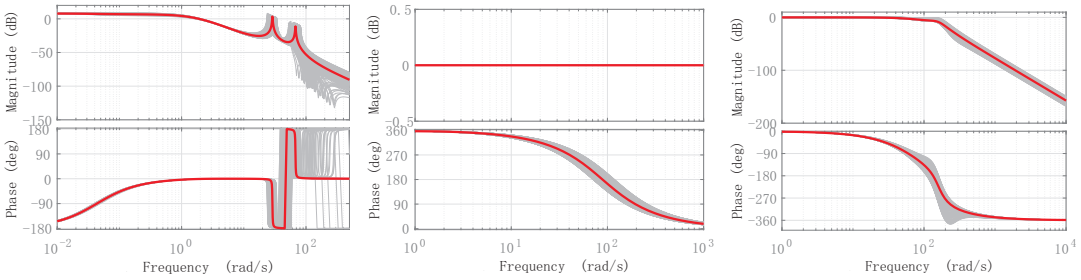

(a) VEGA model (ψ_{INS}/β_ψ) at t = 50 s (b) Delay model ($\beta_{c\tau}/\beta_c(j\omega)$) (c) Actuator model ($\beta_\psi/\beta_{c\tau}(j\omega)$)

Scattered responses Nominal response

FIGURE 5 Bode plots of the uncertain LFT models

Delay LFT model

This LFT model characterizes the delays originated by the digital processing of the on-board computers (12 ms), sensors (12 ms) and TVC actuators (15 ms). All those contributors are modelled through a 2^{nd} order Padé approximation using an uncertain delay defined as $\tau = \tau^0 + \sigma_\tau \delta_\tau$ (with τ^0 = 39 ms and σ_τ = 10 ms). Similarly, this model can be expressed as an upper LFT interconnection $\mathcal{F}_u(G_\tau(s), \Delta_\tau)$, where $G_\tau(s)$ is described in equation 21 and $\Delta_\tau \in \mathbf{\Delta_\tau}$ with $\mathbf{\Delta_\tau} = \{\delta_\tau I_2; \delta_\tau \in \mathbb{R}; ||\delta_\tau||_\infty \leq 1\}$. The bode diagram with the nominal and dispersed responses is shown in Figure 5b.

$$G_\tau(s) = \frac{s^2\tau^2 - s6\tau + 12}{s^2\tau^2 + s6\tau + 12} \tag{21}$$

TVC Actuator LFT model

The TVC actuator model is derived to fit the actuator dynamics obtained from hardware-in-the-loop simulations. This model is also described as an upper LFT interconnection $\mathcal{F}_u(G_{TVC}(s), \Delta_{TVC})$, where $\Delta_{TVC} \in \mathbf{\Delta_{TVC}}$. The reader is referred to reference [11] for a detailed description of this LFT model. The bode plot presenting the nominal frequency response and the LFT coverage is illustrated in Figure 5c.

2.4 | VEGA Control System

The VEGA control system is comprised of two subsystems. First, the TVC subsystem uses measurements from the INS to compute the necessary nozzle deflections to follow the attitude commands from the guidance function. These nozzle deflections are then delivered to two orthogonal nozzle electro-mechanical actuators (lanes *A* and *B*). Second, the RACS consists of six thrusters to control the roll rate and perform a fine three-axis attitude control during the ballistic phase.

During the atmospheric phase, the guidance is performed in open-loop configuration following a pre-programmed trajectory. This flight strategy leads to deviations from the nominal trajectory, which are corrected in upper phases. In addition, due to the high moment of inertia of the launch vehicle along the first phase, the RACS is not able to set the roll rate to zero. As a consequence, the roll rate is only limited, which means the RACS will only act if the roll rate is over a certain threshold.

The VEGA TVC control architecture is shown in Figure 6 [1]. Due to axial symmetry, the same TVC controller is used in pitch and yaw channels. Thus, for each channel, the control law is based on a PD controller to stabilize the launcher's attitude, a lateral control feedback to limit the drift of the vehicle and a set of $H(s)$ filters with different purposes: $H_1(s)$ improves the low-frequency rigid-body stability margins; $H_2(s)$ performs a derivative action to compute the attitude rate error signal $\dot{\psi}_e$; $H_3(s)$ notches the first bending mode and $H_4(s)$ attenuates the upper bending modes.

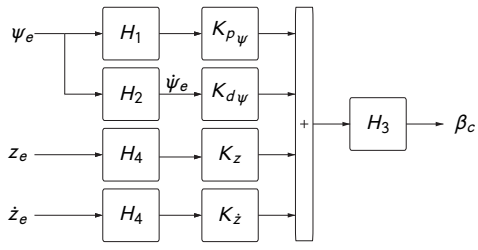

FIGURE 6 VEGA TVC Control Architecture

As aforementioned, in order to cope with the large dynamical system variations, different controllers must be designed along the atmospheric trajectory at distinct operational design points (i.e. every 10 seconds for the VEGA launcher). Then, the controller gains and filters are discretised and scheduled based on the non-gravitational velocity. In this work, the baseline controller used is that for the VEGA VV05 mission.

2.5 | Atmospheric phase VEGA requirements

The TVC subsystem must ensure stability to guidance commands while satisfying very demanding and tight performance requirements in the presence of external disturbances. Furthermore, during the maximum dynamic pressure region, the angle of attack α must be kept small in order to reduce the structural loads on the launch vehicle. The most relevant specifications for the atmospheric phase are listed in Table 2.

TABLE 2 VEGA stability and performance requirements for the atmospheric phase

	Requirements	Metrics		Bounds
Stability Requirements	Rigid-body margins	LF-GM	Nominal	$\geq$ 6 dB
			Dispersed	$\geq$ 0.5 dB
		DM	Nominal	$\geq$ 100 ms
			Dispersed	$\geq$ 40 ms
		HF-GM	Nominal	$\leq$ - 6 dB
			Dispersed	$\leq$ - 3 dB
	Flexible-body margins	GM_f	Nominal	$\leq$ - 3 dB
			Dispersed	$\leq$ - 3 dB
		DM_f	Nominal	$\geq$ 50 ms
			Dispersed	$\geq$ 20 ms
Performance Requirements	Load performance	Q_α		$<Q_\alpha$ envelope
	Lateral control performance	z		<500 m
		$\dot{z}$		<15 m/s
	Actuation performance	β		<6.5 °

Stability requirements are distinguished between rigid- and flexible-body stability margins for nominal and scattered conditions. On the one hand, three rigid-body margins are considered: low-frequency gain margin (LF-GM), delay margin (DM) and high-frequency gain margin (HF-GM). On the other hand, a gain margin (GM_f) and a delay margin (DM_f) are defined for gain- and phase-stabilized bending modes respectively. Note that phase margins are expressed as the equivalent delay at the frequency at which the margin is computed.

Performance requirements are verified via time-domain Monte-Carlo simulations using the nonlinear high-fidelity simulator VEGACONTROL (developed by ELV, and proven to be an industrial-level validation benchmark). The different performance metrics must remain below given bounds in the face of parameter dispersion and disturbances such as noise and wind. The loads requirement is expressed as the product of the dynamic pressure (see Figure 2b) and the angle of attack, $Q\alpha$. This metric must be below a given profile versus Mach. Furthermore, the lateral displacement with respect to the reference trajectory frame shall be limited in the atmospheric phase (both in position z and velocity $\dot{z}$). Finally, the actuator effort shall also be limited to avoid saturation and reduce TVC consumption.

3 | VEGA CONTROL LEGACY RECOVERY

In this section, the structured $\mathcal{H}_\infty$ synthesis technique is applied to the actual VEGA VV05 mission data to recover the baseline rigid-body mission controller. The aim is to provide a first step towards a robust design framework, which is more methodological and offers more design capabilities than the classical design techniques. This recovery also facilitates the transfer of technology to industry as it allows to build exactly from their architecture, and arrive to the same result, strongly building confidence on the process. The VEGA legacy recovery was explored in [20]. However, in this paper, a more suitable closed-loop interconnection for design is proposed. In addition, the main closed-loop transfer functions are analysed analytically to give an understanding on the constraints imposed by the controller structure and facilitate the weighting function selection.

Firstly, the control synthesis is formulated in a robust control design framework. Then, key guidelines on the weighting function selection are provided. Finally, the design is exemplified in a linear design point and validated using VEGACONTROL simulator.

3.1 | Problem formulation

The design model used in this work is illustrated in Figure 7. Note that the main input-output channels of the closed-loop system are scaled by frequency-domain weighting functions represented by shaded blocks. These weighting functions are chosen to impose control requirements on the design and its selection will be discussed in Section 3.2.

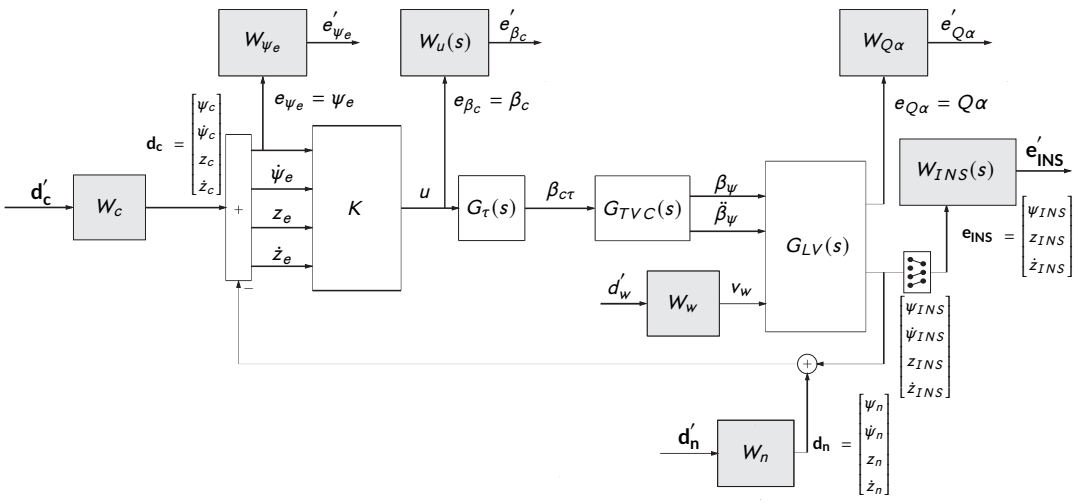

FIGURE 7 Closed-loop diagram for design

It should be mentioned that the closed-loop diagram illustrated in Figure 7 differs from the design interconnections employed in previous works [20, 21], which are based on the real implementation of the VEGA TVC control architecture (see Figure 6) where the attitude error rate signal $\dot{\psi}_e$ is obtained by processing ψ_e through a pseudo-derivative filter $H_2(s)$. Differently, the design model shown in Figure 7 extracts $\dot{\psi}_e$ directly from the launch vehicle model $G_{LV}(s)$. In practice, this additional measurement can be provided by VEGA's INS. This new design architecture offers three main advantages:

1) it simplifies the design diagram, since the pseudo-derivative filter $H_2(s)$ is no longer needed;

2) as a consequence, the size of the closed-loop system is reduced. This also leads to a reduction of the controller size when using non-structured synthesis techniques such as the standard $\mathcal{H}_\infty$ or LPV techniques;

3) finally, this configuration provides better insight into the contribution of each rigid-body gain on the actuation channel. For instance, the effect of K_{p_ψ} and K_{d_ψ} is merged in one single channel from ψ_e in the closed-loop architecture used in previous works, while in the proposed interconnection (see Figure 7), each rigid-body gain has its own channel.

The closed-loop interconnection is composed of 4 main blocks: $G_{LV}(s)$ is the nominal VEGA launcher model, which accounts for rigid-body and nozzle dynamics; K is the controller block, which is composed of the rigid-body gains $\left(K = \begin{bmatrix} K_{p_\psi} & K_{d_\psi} & K_z & K_{\dot{z}} \end{bmatrix}^T\right)$; $G_{TVC}(s)$ and $G_\tau(s)$ represent the nominal actuator dynamics and nominal delay of the system. It should be remarked that the aim is to reproduce the classical design framework, which is performed for nominal conditions. Thus, no uncertainties are used at this design stage. Moreover, since the focus of the design is on the rigid-body gains, $G_{LV}(s)$ does not include the flexible-body motion and the controller K is only composed by the rigid-body gains (the set of filters $H(s)$ is not used during this design stage, although they are added for the time-domain validation stage).

The design architecture presented in Figure 7 can also be expressed as a standard $\mathcal{H}_\infty$ interconnection (see Figure 8), where the main closed-loop interconnections are re-arranged into the generalised plant $P(s)$, and the input and output weighting functions are expressed as W_{in} and W_{out} respectively. The generalised plant $P(s)$ has a set of inputs formed by the commands, wind disturbance and sensor noise inputs $\left(\mathbf{d} = \begin{bmatrix} \mathbf{d_c}^T & d_w & \mathbf{d_n}^T \end{bmatrix}^T\right)$ and a set of outputs $\left(\mathbf{e} = \begin{bmatrix} e_{\psi_e} & \mathbf{e_{INS}}^T & e_{Q\alpha} & e_{\beta_c} \end{bmatrix}^T\right)$, which have been chosen to cope will all the requirements presented in Table 2. In particular, $\mathbf{e}$ is formed by the attitude error ψ_e, the (attitude, drift and drift-rate) INS measurements at node location, the load performance requirement $Q\alpha$ and the commanded actuator deflection β_c. Finally, the scalar u denotes the controller output, while the controller input is represented by the vector $\mathbf{y} = \begin{bmatrix} \psi_e & \dot{\psi}_e & z_e & \dot{z}_e \end{bmatrix}^T$.

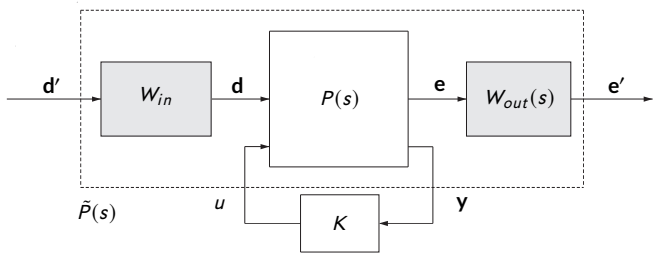

FIGURE 8 $\mathcal{H}_\infty$ interconnection

The transfer function from the inputs $\mathbf{d}$ to outputs $\mathbf{e}$ is generally defined as $\mathcal{T}_{ed} = \mathcal{F}_l(P(s), K)$, where $\mathcal{F}_l$ denotes the lower LFT. In this context, the relation between outputs and inputs can be analysed using the following matrix notation:

$$\left[\begin{array}{c} \psi_e \\ \psi_{INS} \\ z_{INS} \\ \dot{z}_{INS} \\ Q\alpha \\ \beta_c \\ \hline \mathbf{y} \end{array}\right] = \left[\begin{array}{ccc|c} S_\psi & -G_{w\psi} & T_\psi & K_{p_\psi} \\ T_\psi & G_{w\psi} & -T_\psi & G_{u\psi} \\ T_z & G_{wz} & -T_z & G_{uz} \\ T_{\dot{z}} & G_{w\dot{z}} & -T_{\dot{z}} & G_{u\dot{z}} \\ T_{Q\alpha} & G_{wQ\alpha} & -T_{Q\alpha} & G_{uQ\alpha} \\ KS_y & -KG_{wy} & -KS_y & I \\ \hline S_y & -G_{wy} & -T_y & K \end{array}\right] \left[\begin{array}{c} \mathbf{d_c} \\ d_w \\ \mathbf{d_n} \\ \hline u \end{array}\right] \tag{22}$$

where $S_\#$ and $T_\#$ are the sensitivity and complementary sensitivity functions of the corresponding channel #. $S_\#$ is defined as $S_\# = (I + G_\# K)^{-1}$ and $T_\# = I - S_\#$. In addition, $G_{w\#}$ and $G_{u\#}$ represent the transfer functions from the wind disturbance and controller output to the performance indicator #, respectively.

As mentioned before, the control problem is formulated by scaling the generalised plant $P(s)$ through frequency-domain input and output weighting functions forming the augmented generalised plant $\tilde{P}(s)$ (see Figure 8). The input weighting functions are tuned to scale the closed-loop dynamics at the input side with respect to their expected variations $(W_{in} = diag(W_c, W_w, W_n))$. On the other hand, the output weighting functions are shaped to specify the desired requirements $(W_{out} = diag(W_{\psi_e}, W_{\psi_{INS}}, W_z, W_{\dot{z}}, W_{Q\alpha}, W_u))$. Tracking objectives and stability requirements are set on the attitude channel by W_{ψ_e} and $W_{\psi_{INS}}$. Similarly, W_z and $W_{\dot{z}}$ address the lateral control objectives while $W_{Q\alpha}$ adds constraints to satisfy the load requirements. Finally, the actuation performance is limited by W_u. Although not implemented in this work, it should be mentioned that other requirements, such as actuation rate or angular acceleration, can also be considered in the design.

In preparation for the subsequent weight design, all transfer functions in equation 22 have been analytically derived with the aim of identifying key design parameters and facilitating the weighting function selection. However, due to the high order of those transfer functions, it was not possible to perform the same analytical study carried out in [16], where a simpler model of the launch vehicle was analysed in terms of classical design parameters such as the natural frequency ω_n and the damping ratio ζ.

Nevertheless, all transfer functions were analysed in terms of low- and high-frequency asymptotes (see Table 3). This analysis shows that, in addition to the intrinsic physical limitations of the launch vehicle, the structure of the controller also introduces constraints to the system. This study is also very relevant because it gives information on how to shape the weights and it will be used in Section 3.2 for the weighting function selection.

TABLE 3 Low- and high-frequency asymptote analysis.

Transfer function	$\omega = 0$	$\omega = \infty$
ψ_e/ψ_c	1	1
z_{INS}/ψ_c	K_{p_ψ}/K_z	0
$z_{INS}/\dot{\psi}_c$	K_{d_ψ}/K_z	0
z_{INS}/z_c	1	0
$z_{INS}/\dot{z}_c$	$K_{\dot{z}}/K_z$	0
β_c/ψ_c	0	K_{p_ψ}
$\beta_c/\dot{\psi}_c$	0	K_{d_ψ}

Finally, the structured $\mathcal{H}_\infty$ optimisation consists of finding a stabilizing structured controller K that minimises the $\mathcal{H}_\infty$ norm of the cost function given below in equation 23. The $\mathcal{H}_\infty$ norm represents the maximum singular value of the system ($\overline{\sigma}$), which is the generalisation of the eigenvalue for multivariable systems. It can also be interpreted as the maximum gain or amplification of energy from the weighted generalised inputs $\mathbf{d}'$ to the weighted generalised outputs $\mathbf{e}'$.

$$\min_K ||\mathcal{T}_{e'd'}(s)||_\infty = \min_K \max_{\omega\in\mathbb{R}} \overline{\sigma}(\mathcal{T}_{e'd'}(j\omega)) = \sup_{d'\neq 0} \frac{||e'||_2}{||d'||_2} \tag{23}$$

This optimisation process is implemented in MATLAB through the command *hinfstruct* [22]. It should be remarked here that the structured $\mathcal{H}_\infty$ is a non-smooth and non-convex optimiser. This implies the optimisation can be drastically affected by the choice of the controller structure as well as the number of tunable parameters and their initial guesses or initialisations. It is important to remark that the control problem was not initialised using the baseline knowledge (i.e. the baseline controller gains) in order not to influence the optimisation. Rather, it was configured to perform multiple optimisations from a set of 5 random starting points to mitigate the local-minima nature of the structured $\mathcal{H}_\infty$ optimisation.

3.2 | Weighting function selection

The selection of the weighting functions generally implies an iterative process with several heuristic steps to obtain an adequate set of weights. Nevertheless, in this section, some simple guidelines are provided to improve the understanding on how to express the design specifications in the frequency domain. Those guidelines are mainly based on physical properties of the launch vehicle and limitations imposed by the controller structure (see Table 3).

Alternatively, the weighting function selection for the control legacy-recovery process may also be performed based on the inverse of the closed-loop transfer functions using the baseline controller. This reverse-engineering process may result in a faster approach, nevertheless, it would require more complex weighting functions, and more importantly for the scope of this recovery exercise, it does not provide any analytical insight into the system limitations (physical and controller). Nonetheless, note that the baseline closed-loop transfer functions were subsequently employed as reference to fine-tune the analytically-selected weighting functions in order to exactly recover the baseline controller.

In the standard $\mathcal{H}_\infty$ framework, the order of the controller equals the order of the scaled generalised plant $\tilde{P}(s)$, thus, the order of the weighting functions is traditionally kept low to avoid high-order controllers. On the other hand, using the structured $\mathcal{H}_\infty$ technique, this restriction is no longer applicable since the controller size is fixed. Nevertheless, for ease of tuning and simplicity, constant and first order weighting functions are used.

3.2.1 | Input weighting functions

Proper scaling of the input channels is key for a good control design, particularly working with multivariable systems. It is also relevant the use of suitable units to balance the different channels (e.g. expressing angles in degrees instead of radians).

Firstly, the commanded input matrix W_c is described in equation 24. In this work, W_{ψ_c} has been fixed to consider a maximum attitude angle command of 1 deg and $W_{\dot{\psi}_c}$ is tuned to balance the attitude and attitude rate channels. Similarly, W_{z_c} is adjusted to balance the lateral feedback channels. Using the information from Table 3, a suitable scaling is achieved using the following relations: $W_{\dot{\psi}_c} \approx K_{p_\psi}/K_{d\psi}$ and $W_{z_c} \approx K_{\dot{z}}/K_z$. Those weights were used as initial values and then a manual fine-tuning was required to recover the baseline controller at every design point.

$$W_c = \begin{bmatrix} \frac{\pi}{180} W_{\psi_c} & 0 & 0 & 0 \\ 0 & \frac{\pi}{180} W_{\dot{\psi}_c} & 0 & 0 \\ 0 & 0 & W_{z_c} & 0 \\ 0 & 0 & 0 & W_{\dot{z}_c} \end{bmatrix} \tag{24}$$

The input disturbance weight W_w aims to scale the wind channel with respect to the maximum expected wind speed. For the legacy recovery, this weight has been fixed for a maximum wind of 10 m/s.

Finally, the input noise weight W_n models the sensor noise of each feedback measurement (see equation 25). The expected noise levels from the IMU sensor used by VEGA are W_{ψ_n} = 0.02 deg and $W_{\dot{\psi}_n}$ = 0.1 deg. For the lateral deviation measurements, the estimated errors provided by the guidance function are W_{z_n} = 0.01 m for the drift and $W_{\dot{z}_n}$ = 0.001 m/s for the drift-rate.

$$W_n = \begin{bmatrix} \frac{\pi}{180} W_{\psi_n} & 0 & 0 & 0 \\ 0 & \frac{\pi}{180} W_{\dot{\psi}_n} & 0 & 0 \\ 0 & 0 & W_{z_n} & 0 \\ 0 & 0 & 0 & W_{\dot{z}_n} \end{bmatrix} \tag{25}$$

3.2.2 | Output weighting functions

W_{ψ_e} and $W_{\psi_{INS}}(s)$ enforce tracking and stability requirements. ${W_{\psi_e}}^{-1}$ and $W_{\psi_{INS}}(s)^{-1}$ bound respectively the classical sensitivity and complementary sensitivity functions of the yaw attitude channel. The two weighting functions are given by:

$$W_{\psi_e} = \frac{180}{\pi}\left(||S_\psi(s)||_\infty\right)^{-1} \tag{26}$$

$$W_{\psi_{INS}}(s) = \frac{180}{\pi}\left(\frac{h_\psi s + \omega_\psi}{s + \frac{\omega_\psi}{l_\psi}}\right)^{-1} \tag{27}$$

where $||S_\psi(s)||_\infty$ is the maximum peak of the sensitivity function of the attitude channel, l_ψ and h_ψ are the low- and high-frequency asymptotes of a low-pass filter and ω_ψ is the filter bandwidth.

Generally, ${W_{\psi_e}}^{-1}$ is chosen as a high-pass filter, with a small low-frequency asymptote to keep low the steady-state tracking error. Nevertheless, due to the inclusion of the lateral control feedback, the steady-state tracking error of the system is fixed to 1 (see Table 3). Thus, in this work, $S_\psi(s)$ is only limited by a constant weighting function to keep small the maximum peak of the sensitivity function to assure good stability margins. Recall that $||S_\psi(s)||_\infty$ directly yields a lower bound on the classical stability gain margin (GM) and phase margin (PM) through the following relations [23]:

$$GM \geq \frac{||S_\psi(s)||_\infty}{||S_\psi(s)||_\infty - 1} \tag{28}$$

$$PM \geq 2\arcsin\left(\frac{1}{2||S_\psi(s)||_\infty}\right) \tag{29}$$

It is also important to note that, as described in equation 27, $W_{\psi_{INS}}(s)^{-1}$ is shaped instead as a low-pass filter. The filter bandwidth ω_ψ should be sufficiently high to have an adequate attitude tracking but low enough to avoid interactions with the first bending mode. For the recovery of the baseline controller, ω_ψ has been fixed to 20 rad/s. Note that this value has been chosen much higher than the attitude control bandwidth to avoid over constraining the optimisation process. In addition, h_ψ is set to a gain of -60 dB to attenuate the control performance at high frequencies and minimise the noise contribution. Finally, in order to reduce the number of weight parameters to tune during the design process, l_ψ equals $||S_\psi(s)||_\infty$.

$W_{z_{INS}}$ and $W_{\dot{z}_{INS}}$ specify the lateral control requirements on the design process. Their inverses must refer to the maximum drift and drift rate output expected values. Note that the ratio K_{p_ψ}/K_z imposes a lower bound for ${W_{z_{INS}}}^{-1}$ (see Table 3).

$$W_{z_{INS}} = \left(z_{max}\right)^{-1} \tag{30}$$

$$W_{\dot{z}_{INS}} = \left(\dot{z}_{max}\right)^{-1} \tag{31}$$

The load requirements are set through the weighting function $W_{Q\alpha}$. In this case, ${W_{Q\alpha}}^{-1}$ bounds the maximum angle of attack as follows:

$$W_{Q\alpha} = \frac{180}{\pi}\left(Q\alpha_{max}\right)^{-1} \tag{32}$$

Finally, $W_u(s)$ adds constraints on the actuation performance. In this case, ${W_u}^{-1}$ is shaped as a low-pass filter given by:

$$W_u(s) = \frac{180}{\pi}\left(\frac{h_u s + \omega_u}{s + \frac{\omega_u}{l_u}}\right)^{-1} \tag{33}$$

where l_u and h_u are the low- and high-frequency asymptotes and ω_u is the actuation bandwidth. l_u is tuned to be the maximum expected actuator deflection β_{max} at the design point and the actuation bandwidth has been fixed to $\omega_u = 30$ rad/s. Also note that the controller structure fixes the value of h_u to K_{p_ψ}.

3.3 | Structured $\mathcal{H}_\infty$ Linear Design Point

In this section, the baseline controller recovery using the structured $\mathcal{H}_\infty$ synthesis approach is illustrated at a linear design point, t = 50 s (i.e. around maximum dynamic pressure).

Following the guidelines presented in Section 3.2, the weighting functions are tuned in an iterative process to get the same rigid-body gains as the baseline controller employed in the VEGA VV05 mission. Specifically, the rigid-body gains obtained present less than 1% of error with respect to the baseline controller gains.

To validate the design, the bode plots of the system using the baseline controller (in solid black) and the structured $\mathcal{H}_\infty$ design (in dashed blue with square markers) are shown in Figure 9. This plot also illustrates in green the inverse of the output weighting functions used for this design. It should be remarked that the frequency responses have been multiplied by the input weighting functions and that only a subset of channels are shown for ease of visualization.

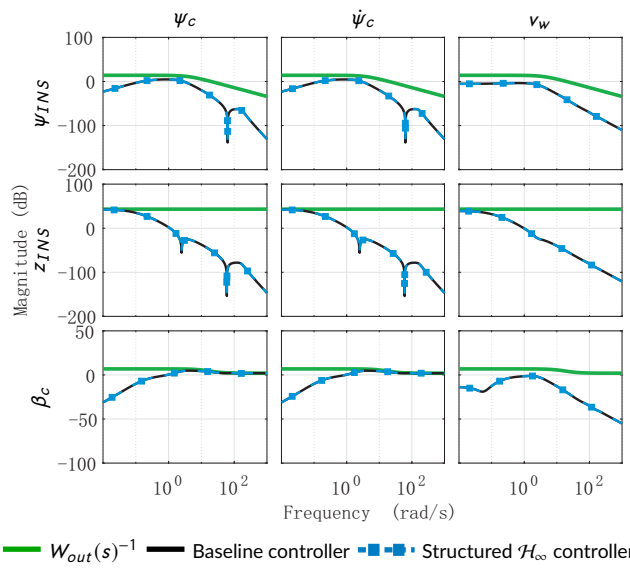

FIGURE 9 Bode plots comparison at t = 50 s: baseline controller Vs structured $\mathcal{H}_\infty$ controller

Looking at Figure 9, it can be observed that the baseline controller is successfully recovered at t = 50 s. This figure shows clearly the upper bound defined by the weighting functions.

The same design procedure is repeated for the rest of the linear design points along the atmospheric flight. Due to the wide dynamic variation of the launch vehicle model, a different set of weighting functions is needed to recover the baseline controller at each grid design point (but note that the weights used for the design at t = 50 s are used as the basis for the weights in all the other points). In total, 9 structured $\mathcal{H}_\infty$ controllers have been synthesized starting at t = 5 s and then at every 10 seconds between the flight instants t = 20 s and t = 90 s. Similarly, in all the design points, the rigid-body gains synthesized exhibit less than 1% of error with respect to the baseline controller gains.

Although not covered in this paper, the proposed recovery design methodology can also be used to recover the baseline bending filters. Nonetheless, it is highlighted that this task would be much more complex for several reasons. First, it would be necessary to parametrise the bending filters to apply the structured $\mathcal{H}_\infty$ optimisation technique. In addition, some of the weighting functions would have to be of higher order to shape the filters' dynamics, which implies more tuning effort to achieve a total recovery. A good example of how the proposed structured $\mathcal{H}_\infty$ framework can be augmented to jointly design the rigid-body controller and the bending filters is given in reference [24].

3.4 | Nonlinear verification

Finally, the 9 structured $\mathcal{H}_\infty$ controllers are scheduled, implemented and verified in the nonlinear high-fidelity simulator *VEGACONTROL*. The final scheduled structured $\mathcal{H}_\infty$ controller is obtained using the same scheduling scheme employed for the VEGA baseline controller, that is through linear interpolation using the non-gravitational velocity as the scheduling parameter. Although not used in the design process, the flexible-body motion of the vehicle as well as the H filters of the TVC control architecture (see Section 2.4) are implemented for the nonlinear, time-domain simulations. Also note that the estimated wind from the VEGA VV05 mission is used in this analysis.

Figure 10 shows the load performance indicator $Q\alpha$ for nominal flight conditions (those encountered during the selected mission, i.e. VV05 [15]). It is seen that the loads suffered by the launch vehicle during this mission using the baseline controller (in solid black) are below the given $Q\alpha$ safety envelope depicted in dot-dashed red for the whole atmospheric flight. Nonetheless, a noticeable peak is observed around Mach 3, which is close to the safety envelope. In essence, this peak is produced by a strong wind gust encountered around t = 60 s.

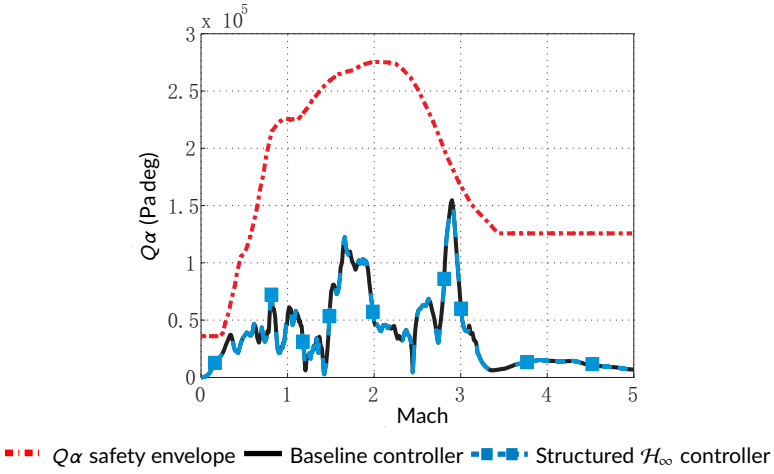

FIGURE 10 VEGA legacy recovery nonlinear validation

Figure 10 clearly illustrates that the control behaviour of the scheduled baseline controller for the VEGA atmospheric phase is successfully recovered using the structured $\mathcal{H}_\infty$ synthesis technique (again, no discernible difference is observed in the responses). As a summary, it is noted that this legacy-recovery design process is not trivial and it requires a good understanding of the physics of the launch vehicle as well as the constraints introduced by the controller structure into the system. For the latter, it is paramount to reconcile the closed-loop transfer functions of the system with the frequency-dependent weighting functions (i.e. via the asymptote analysis performed in Section 3.1). Nonetheless the difficulty, this successful demonstration greatly advances the case for the use of this more methodological robust design tools over the classical design approach (especially, or at least, for launcher TVC design).

4 | CONTROL DESIGN AUGMENTATION

This section explores the room for improvement offered by the structured $\mathcal{H}_\infty$ design framework as it allows providing the optimiser with more information about the system. First, the impact of including a wind turbulence model in the design process is analysed and accounted for in the design. Then, the design is augmented by taking parametric uncertainties into account.

4.1 | Wind generator augmentation

The effect of wind disturbance is a critical factor for any launcher atmospheric phase [25, 26]. It generally produces a significant degradation in the global performance of the mission and it induces structural loads which can cause loss of vehicle. In this regard, the controller must minimize the contribution from the wind disturbance while satisfying stability and performance requirements (see Section 2.5).

In this section, the wind channel transfer functions are analysed to have a better understanding on the controller capabilities to reduce the disturbance action. Then, the structured $\mathcal{H}_\infty$ design framework presented in Section 3 is augmented by incorporating a wind turbulence model, which accounts for real wind levels in the controller synthesis. Finally, a nonlinear benchmark is presented to evaluate the influence of this proposed wind model.

4.1.1 | Wind disturbance analysis

Classical control design techniques generally do not implicitly consider any wind model during the design process. The wind disturbance rejection is normally evaluated using an extensive nonlinear analysis coverage with a set of different wind profiles. Differently, the robust control design framework presented in Section 3 allows to tackle the design considering multiple competing system requirements while also taking the wind disturbance contribution into account. This is quite relevant for design, since the wind rejection performance drives the main traditional control strategies considered in the literature for launch vehicle control synthesis (i.e. attitude-error-minimum, drift-minimum and load-minimum) [26, 27, 28, 29]. Those control modes attempt to cancel out the steady-state values of each of those three performance metrics from the wind disturbance input.

To evaluate the characteristics of the steady-state wind disturbance rejection for the VEGA launcher, the transfer functions from the launcher wind input v_w have been derived and their low-frequency asymptotes are given in Table 4. It is critical to notice that only the steady-state value of the drift-wind channel can be minimised (by using a low gain ratio K_{p_ψ}/K_z). Note that the minimum-drift condition can be achieved using $K_{p_\psi} = -\frac{l_{CP}}{l_{CP}+l_{CG}}\frac{T-D}{l}$, but this choice leads to an unstable response. Differently, the other steady-state values only depend on physical parameters of the launch vehicle, and thus they cannot be set to zero or controlled in any way. This feature can only be enhanced by including new sensors and feedback loops to the TVC control system (i.e. angle of attack), which implies changing the control law.

TABLE 4 Low-frequency asymptote analysis of the wind disturbance channel.

Transfer function	$\omega = 0$
$\psi_{INS}/v_w(s)$	$\frac{1}{V}\frac{N(l_{CP}+l_{CG})}{N(l_{CP}+l_{CG})+l_{CG}(T-D)}$
$z_{INS}/v_w(s)$	$\frac{1}{V}\frac{K_{p_w}TN(l_{CP}+l_{CG})+Nl_{CP}(T-D)}{K_zT[N(l_{CP}+l_{CG})+l_{CG}(T-D)]}$
$Q\alpha/v_w(s)$	$-\frac{Q}{V}\frac{l_{CG}(T-D)}{N(l_{CP}+l_{CG})+l_{CG}(T-D)}$
$\beta_c/v_w(s)$	$-\frac{1}{V}\frac{1}{T}\frac{Nl_{CP}(T-D)}{N(l_{CP}+l_{CG})+l_{CG}(T-D)}$

Despite the fact that most of the wind steady-state responses cannot be controlled for the VEGA launcher, the transient response also plays a significant role on the system. In this regard, it is very important to scale properly the wind channel with respect to the wind levels that the launcher will encounter in the real flight. In the authors' opinion, the use of statistical wind models in the design process will certainly guide the optimiser to obtain an overall better disturbance rejection performance. Next, a wind turbulence model is proposed to be considered in the design process.

4.1.2 | Wind generator description

In this study, following the criteria found in [30] and the work of [11], the wind disturbance velocity v_w is modelled by coloring white noise n_w through a Dryden filter with the following transfer function:

$$G_w(s) = \frac{v_w}{n_w}(s) = \frac{\sqrt{\frac{2}{\pi}\frac{V(h)-v_{wp}(h)}{L(h)}\sigma^2(h)}}{s+\frac{V(h)-v_{wp}(h)}{L(h)}} \tag{34}$$

where $L(h)$ and $\sigma(h)$ are the turbulence length scale and the standard deviation versus altitude h. The values of $L(h)$ and $\sigma(h)$ are given in tabular-form in [30] for light, moderate and severe turbulence. Finally, the build-up wind speed profile envelope $v_{wp}(h)$ is defined in equation 35 and illustrated in Figure 11a. This altitude profile is defined by an exponential leading edge and a 1-cosine shape trailing edge for low and high altitudes respectively. For intermediate altitudes, the profile is described by a constant gust amplitude A. In this work, the envelope is characterized for the first 20 km of altitude (H_f = 20000 m), which is the altitude range where the wind disturbance plays the most significant role in performance metrics such as $Q\alpha$. The profile amplitude is set to A = 14 m/s and the thickness of the initial and final edges are H_l = 2000 m and H_u = 2500 m. The previous values have been chosen to fit the model with a range of different wind profiles (see Figure 11b).

$$v_{wp}(h) = \begin{cases} 10A[(\frac{h}{H_l})^{0.9} - 0.9\frac{h}{H_l}] & \text{for} \quad 0 \le h < H_l \\ A & \text{for} \quad H_l \le h \le H_f - H_u \\ \frac{A}{2}[1 - cos(\frac{\pi}{H_u}(h - H_f))] & \text{for} \quad H_f - H_u < h \le H_f \end{cases} \tag{35}$$

As shown in [11], $G_w(s)$ combined with the planar wind steady-state profile $v_{wp}(h)$ is able to cover the estimated wind encountered in the VEGA VV05 mission. This analysis is extended here to other different winds (see Figure 11b). It is shown that a set of 1000 random samples of this wind configuration (depicted in grey) covers the range of 4 different real wind data (extracted from real measurements taken at the VEGA launch site).

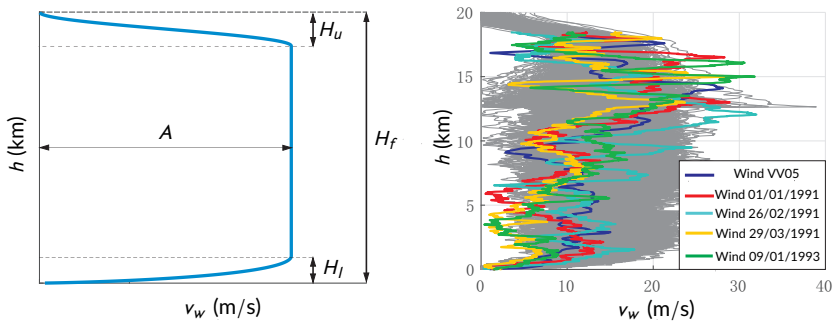

(a) Planar wind steady-state profile $v_{wp}(h)$ (b) Wind profile analysis with real wind data

FIGURE 11 Design wind speed profile envelope

$G_w(s)$ has been successfully used for analysis in [11]. The aim here is to use the model for design, providing the optimiser information about the frequency content of the wind disturbance. This characteristic is very important in frequency-domain synthesis techniques such as the structured $\mathcal{H}_\infty$ technique.

The wind model is implemented at the wind disturbance input of the launch vehicle model. Using this configuration, the input disturbance weight W_w now scales the Gaussian process described by the Dryden filter $G_w(s)$. This input weighting function is defined as $W_w = \sigma_w$, where σ_w is the standard deviation of the unitary white noise input n_w. In this work, σ_w is assumed to be 3 so that 99.7% of the wind levels are considered in the design.

4.1.3 | Wind generator assessment

To evaluate the influence of the wind model $G_w(s)$ on design, two different controllers are synthesized using the structured $\mathcal{H}_\infty$ technique, one for moderate and the other for severe wind levels. Both controller designs are performed using the same weighting functions (those used to recover the baseline controller in Section 3) at the same 9 operating points. Note that in these designs only the rigid-body gains are optimised, while the bending filters are kept the same as the baseline controller.

The synthesized rigid-body gains are compared with the baseline in Figure 12. Note that the values in the y axis are not provided for confidential reasons. Looking at Figures 12a and 12b, it is observed that the attitude gains of the three designs present the same trend but with slightly different values. It is also shown that the optimiser yields higher lateral feedback gains for the severe-wind design than for the other two cases (see Figure 12c and 12d).

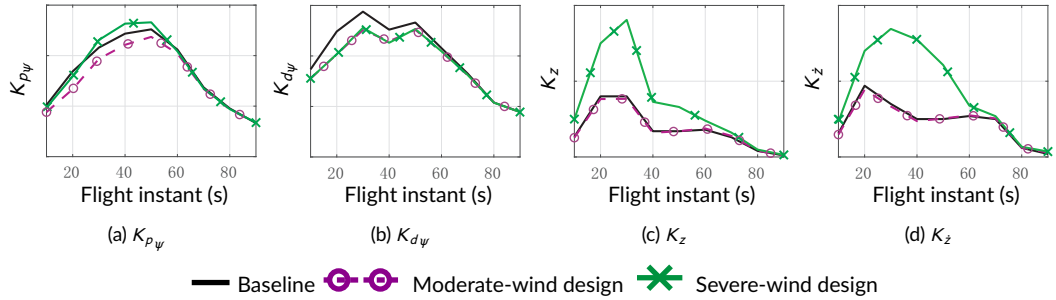

(a) K_{p_ψ} (b) K_{d_ψ} (c) K_z (d) $K_{\dot{z}}$

FIGURE 12 Time-evolution of the synthesized rigid-body gains

In particular, the increase of $K_{\dot{z}}$ reduces the wind disturbance transient energy of the $Q\alpha$ channel (recall from equation 5 that the angle of attack directly depends on the drift-rate). This effect on the load alleviation is illustrated in Figure 13a, where the $Q\alpha$-wind frequency responses of the severe-wind design at t = 50 s are compared using different drift-rate gains. Nevertheless, the increase of $K_{\dot{z}}$ must be handled with care since it deteriorates the stability margins as it can be seen in Figure 13b. This plot shows the effect of $K_{\dot{z}}$ on the rigid-body gain margins for the severe-wind design at t = 50 s. Note that all values are normalised with respect to the margins of the actual severe-wind design. It is observed that using three times the drift-rate gain generates a loss of 2.5 dB at LF-GM and 0.6 dB at HF-GM.

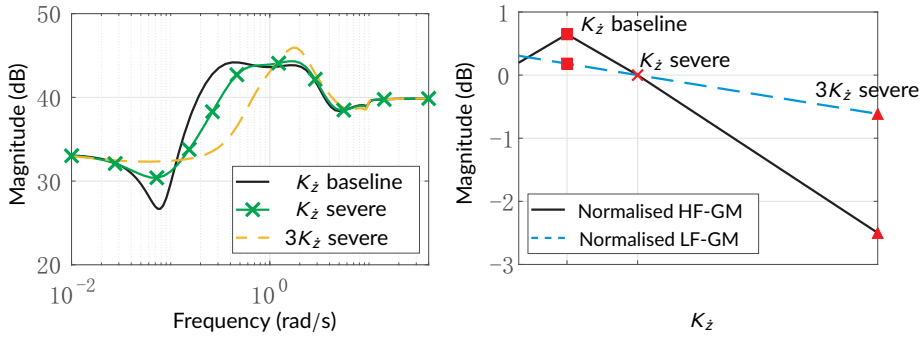

(a) Bode plot of the $Q\alpha$-wind channel with different drift-rate gains at t = 50 s

(b) Normalised rigid-body gain margins versus $K_{\dot{z}}$ at t = 50 s

FIGURE 13 Analysis of the effect of $K_{\dot{z}}$ on the severe-wind design

This behaviour is confirmed in the high-fidelity, nonlinear simulator. Figure 14 shows a comparison of the two augmented designs versus the baseline controller using for all the nominal flight as well as the VV05 mission wind data.

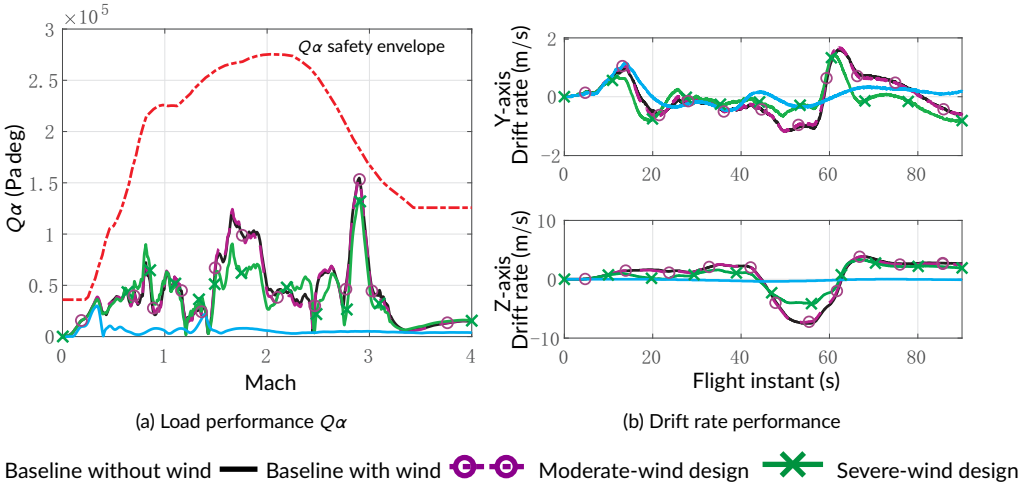

(a) Load performance $Q\alpha$

(b) Drift rate performance

FIGURE 14 Nominal nonlinear flight responses

Looking at Figure 14, it is interesting to observe that the moderate-wind design (in dashed magenta with circle markers) almost perfectly matches the baseline controller responses. Furthermore, in order to illustrate the impact of the wind input on performance indicators such as $Q\alpha$ or drift-rate, the nonlinear response of the baseline controller without wind is also compared. It is highlighted by comparing both baseline simulations that the structural loads and drift-rate performance are highly influenced by the wind disturbance. Thus, since the wind characteristics change with every mission, this comparison highlights the importance of being robust against a large range of wind profiles.

Finally, as it was expected, the severe-wind design (in solid green with cross markers) reduces the aerodynamic loads (see Figure 14a). Particularly, the maximum $Q\alpha$ peak around Mach 3 is reduced by 13% with respect to the baseline controller. Moreover, the drift-rate responses (see Figure 14b) are also significantly improved for the severe-wind controller resulting in less lateral deviations along the flight. It is highlighted that the same benchmarking was performed using different wind profiles, obtaining the same wind disturbance rejection capabilities shown in Figure 14.

Overall, it is observed that the structured $\mathcal{H}_\infty$ optimiser results in better controllers (in terms of wind disturbance rejection) when stronger wind levels are employed in the design process. Recall that the same weighting functions were used for the three controllers presented. For a finer synthesis, the weighting functions could be tailored according to the main controller objective at each linear design point.

4.2 | Robust design augmentation

In this section, the structured $\mathcal{H}_\infty$ design interconnection is further augmented by taking parametric uncertainties into account, and a new structured $\mathcal{H}_\infty$ design is performed. The resulting controller is analysed in terms of the classical stability margins, the structured singular value μ and nonlinear MC simulations.

4.2.1 | Problem formulation

The previous design interconnection can be further augmented by including uncertainties in the design model. To that end, the nominal LTI models of the TVC actuator, delay and launch vehicle are replaced by the LFT models presented in Section 2.3. The resultant standard $\mathcal{H}_\infty$ interconnection is shown in Figure 15. Note that the uncertainty block Δ is pulled out of the generalised plant $P(s)$ and $\Delta \in \mathbf{\Delta}$ with $\mathbf{\Delta} = diag(\mathbf{\Delta_{LV}}, \mathbf{\Delta_{\tau}}, \mathbf{\Delta_{TVC}})$. In addition, the wind turbulence model $G_w(s)$ is also included in $P(s)$.

In this case, the structured $\mathcal{H}_\infty$ control problem consists of finding a stabilizing structured controller K that minimises the cost function $\min_K ||\mathcal{F}_l(\tilde{P}(s,\Delta), K)||_\infty$. It is important to highlight that in this case the control optimisation is performed taking into account any uncertainty combination Δ in the uncertainty set $\mathbf{\Delta}$.

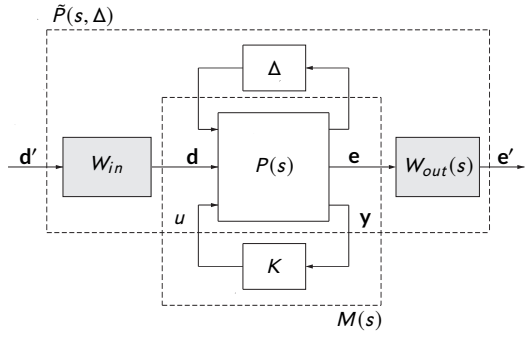

FIGURE 15 Robust standard $\mathcal{H}_\infty$ interconnection

4.2.2 | Robust structured $\mathcal{H}_\infty$ control design

The previous configuration allows to synthesize a controller K that is robust against the expected variations of the main parameters of the system. Furthermore, as shown before, the inclusion of the wind generator model $G_w(s)$ guides the control optimisation to reduce the wind disturbance contribution in the presence of strong wind levels.

As aforementioned, at different phases of the atmospheric flight the design can be tailored to focus on three main different strategies:

- *Tracking performance:* the control system will minimise the attitude deviations from the open-loop guidance commands. However, this approach leads to lateral deviations from the trajectory and it does not account for wind-induced structural loads.
- *Drift performance:* this design scheme aims at minimising the drift in response to wind gusts. In this case, the control system will attempt to generate an attitude response so the normal forces are cancelled out. The drawbacks of this approach are attitude deviations and as in the previous case, high structural loads.
- *Load performance:* the main objective of this approach is to minimise the wind-induced structural loads. To that end, the vehicle will turn into wind to reduce the angle of attack α, leading to attitude deviations and also translational dispersions with respect to the pre-programmed trajectory.

For this final design an optimal control strategy is performed, which means that the system achieves a trade-off balance for the best global performance. In particular, a load-relief control mode is employed about the maximum dynamic pressure region (t = 40-60 s). For the rest of the operating points, the design is focused on minimising the tracking error while keeping the lateral deviations bounded within specifications.

The weight setup follows the same rationale presented in Section 3.2, but differs in the value of the weights, which are tailored in an iterative process to obtained a balanced performance. In addition, they are shaped so the nominal and dispersed stability requirements are satisfied.

As before, the structured $\mathcal{H}_\infty$ synthesis approach is applied at different linear operating points, i.e. every 10 seconds between flight instants t = 20 s and t = 90 s. But different to the previous designs, the controller at t = 5 s is kept the same as the baseline controller because the control design at this point focuses on the vertical flight phase and the start of the pitch over manoeuvre, which have different control requirements.

4.2.3 | Linear analysis

In this section, the system stability is assessed via classical stability margins and the structured singular value μ.

Classical stability analysis

The system stability is traditionally analysed through a set of gain and phase margins at different crossing frequencies (see Section 2.5). These stability margins are analysed in the frequency domain through Nichols plots at different flight times. To that end, the open-loop system (controller, actuator and launch vehicle models) is re-arranged and broken at the controller output in order to reduce the system to a single-input/single-output (SISO) system.

The traditional design verification and validation for the VEGA launcher defines specifications for nominal and dispersed conditions. Firstly, the system stability using the structured robust design is analysed under nominal conditions at the linear design points (see Figure 16a). It can be seen the structured $\mathcal{H}_\infty$ controller provides satisfactory margins throughout the flight satisfying the nominal stability specifications.

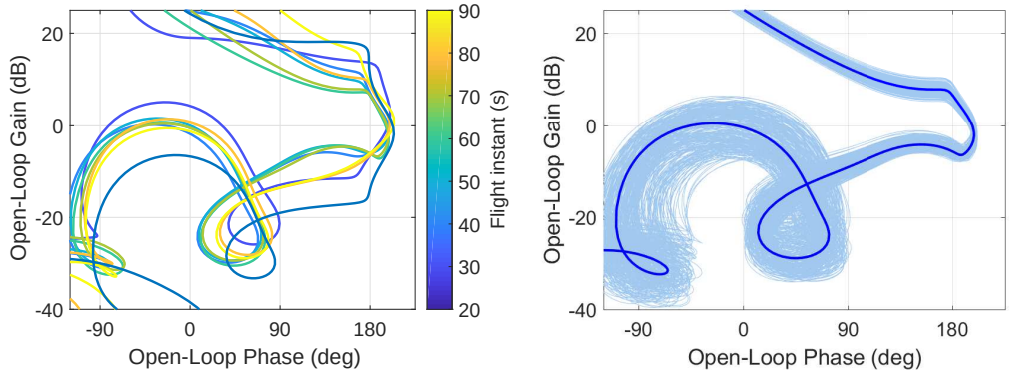

(a) Nominal Nichols charts

(b) Nichols chart at t = 60 s (Nominal Dispersed)

FIGURE 16 Classical stability analysis for the robust structured $\mathcal{H}_\infty$ design

The analysis for scattered configurations is performed using a Monte-Carlo (MC) approach with 1000 random samples (note that in this case the MC is performed on the LFT model as opposed to the VEGACONTROL). Figure 16b shows the Nichols chart of the nominal system at t = 60 s and the 1000 MC random LFT samples. It can be observed the stability degradation due to system uncertainties. In Figure 17, the main linear metrics from Table 2 are shown along different flight times for the nominal LFT as well as for the LFT obtained using at each flight instance the "worst-case" among all the MC runs (these cases are referred to as "MC-based WC" in the plot). It is important to remark that all the stability specifications are fulfilled with the new robust design.

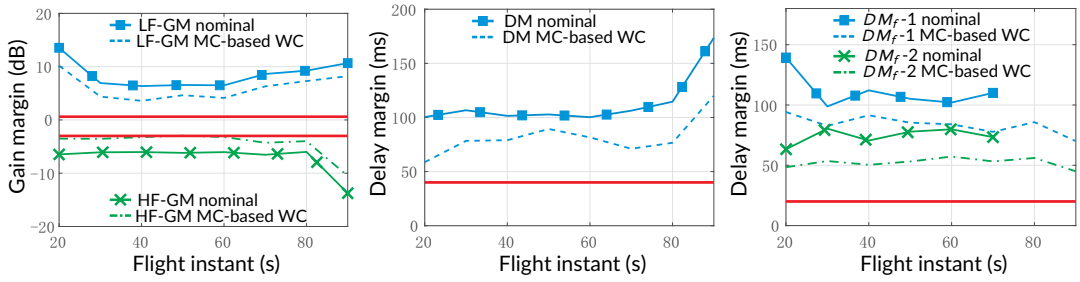

(a) Rigid-body gain margins

(b) Rigid-body delay margin

(c) Flexible-body delay margins

FIGURE 17 Worst-case stability margin assessment (margin requirements for dispersed conditions)

The traditional validation process further extends the previous analyses by using ad-hoc test cases to complete the coverage of the analysis, resulting in an expensive (in terms of both cost and time) procedure. Another practical limitation of the traditional approach is the lack of guarantees in finding worst cases (WCs). This can be overcome by complementing the MC approach by using worst-case tools such as the structured singular value μ, which allows to identify linear WCs and also to evaluate the robustness of the design due to model uncertainties providing analytically guaranteed bounds on robust stability (RS). Note that although there are no guarantees that the linear WCs identified by μ will lead to nonlinear WCs, it is well-known (see references [17, 11]) that if a proper LFT modelling is employed then μ-WCs generally represent critical nonlinear scenarios. Next, this robust analysis technique is presented and applied to the VEGA launcher.

Robust stability analysis

The robust stability of the VEGA launcher system defined by $M(s)$ (see Figure 15) is assessed via the structured singular value μ [19], which is computed as follows:

$$\mu_{\Delta}(M_{11}) = \frac{1}{min_{\Delta}\{\overline{\sigma}(\Delta) : det(I - M_{11}\Delta) = 0\}} \quad \text{with} \quad ||\Delta||_{\infty} < 1 \tag{36}$$

In this context, the system $M(s)$ is then robustly stable if $M(s)$ is nominally stable and the following RS condition is satisfied over all frequencies:

$$\mu_{\Delta}\big(M_{11}(j\omega)\big) < 1, \quad \forall\ \omega \in \mathbb{R} \tag{37}$$

If robust stability is achieved, then there are analytical guarantees that there is no combination of uncertainties within the range defined by the LFT model which leads to instability. It is important to mention that the structured singular value computation is a non-polynomial hard problem. Thus, μ is computed using lower and upper bounds (LB and UB) [19]. The upper bound provides the maximum size perturbation for which the RS condition shown in equation 37 is violated. On the other hand, the lower bound provides the minimum size perturbation for which the RS condition is guaranteed. Note that for this analysis, the uncertainty matrix Δ has been modified to include a 1% complex uncertainty to one of the TVC uncertain parameters. This mixed real-complex uncertainty structure improves the accuracy of the μ computation [19].

Figure 18a shows the upper and lower bounds of μ computed at the same time instance as before, t = 60 s, for two different controllers: the baseline and the last robust structured design. Looking at the baseline μ bounds (in black), it is clear that the system is not robustly stable since there is a peak around 10 rad/s in which both upper and lower bounds are higher than 1. It is highlighted that μ does not only output a binary solution (either the system is robust stable or not), but also provides information in the frequency domain about how the system stability is degraded due to system uncertainties. For instance, it is identified that the peak above 1 is centered around the HF-GM frequencies. This information is quite valuable for synthesis, since it identifies stability problems before going for an extensive MC-based validation process.

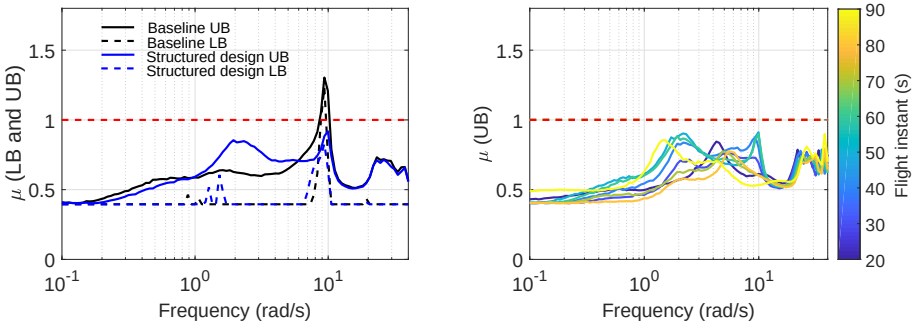

(a) Robust stability analysis at t = 60 s

(b) Robust stability analysis (Structured $\mathcal{H}_{\infty}$ design)

FIGURE 18 Robust stability analysis (RS condition)

On the other hand, Figure 18a clearly shows that using the new augmented structured $\mathcal{H}_\infty$ controller the RS condition is satisfied at all frequencies. Looking at the upper bounds, this robust design slightly improves the RS at low frequencies (below 1 rad/s) and critically much more at high frequencies particularly around the peak at 10 rad/s. These improvements come at the expense of larger upper bounds around 2 rad/s (this illustrates the so-called water-bed effect [19, 23]).

The same RS analysis is carried out at the other linear design points but only for the structured $\mathcal{H}_\infty$ design (see Figure 18b). For ease of visualization, only the upper bounds are shown. As before, this plot clearly shows that the system is robustly stable throughout the atmospheric phase.

4.2.4 | Nonlinear analysis

Finally, all the individual, full augmented (wind and uncertainties) structured $\mathcal{H}_\infty$ controllers from Section 4.2 are scheduled, implemented and validated in the VEGACONTROL simulator. To evaluate the performance and robustness of this design, four MC campaigns of 500 runs are performed. For each run, the same nominal VEGA VV05 flight trajectory is used but the system parameters are all sampled randomly. Each of the four MC campaign uses the same parameters' scattering but a different wind profile (among them, the estimated wind encountered in VEGA VV05 mission – which was also used in the previous figures/comparisons). Note that the four wind profiles have been extracted from real measurements taken at the VEGA launch site (French Guyana) and cover strong and moderate wind gusts at different altitudes. The same four MC set-ups are applied also to the VEGA VV05 baseline controller.

The outcomes of this MC campaign for both controllers are depicted side-by-side in Figure 19 (on the left for the baseline and on the right for the augmented structured design). For each, the total 2000 randomly sampled MC responses are shown for the aerodynamic load $Q\alpha$ (top plots) and the TVC actuator deflections (bottom plots). In order to have a reference, the nominal simulations using the VEGA VV05 mission wind are highlighted in darker lines. Looking at the $Q\alpha$ responses, it can be observed that the higher $Q\alpha$ peaks (around Mach 1.5, 2.5 and 2.9) are reduced for the structured $\mathcal{H}_\infty$ design. As for the TVC actuation, although less visible, the responses using the structured $\mathcal{H}_\infty$ controller require slightly less TVC deflections to handle the different strong wind gusts encountered.

In order to quantitatively compare both designs, a set of performance indicators (such as actuation, attitude error, drift or aerodynamic load performance) are analysed using two different metrics: the ∞-norm and the 2-norm. The former is equivalent to the maximum value taken by the assessed variable, whereas the latter accounts for the energy of the indicator. Figure 20 shows the average of those two norms normalised with respect to the baseline controller values. Overall, it can be seen that the augmented structured $\mathcal{H}_\infty$ design improves the performance for all the indicator/norm pairs. This robust controller reduces the $Q\alpha$ peaks by 10%, the energy of the attitude error also by 10% in both axes and the drift-rate performance is significantly improved by 20% in both ∞- and 2-norms. Furthermore, the average TVC deflection peaks are reduced by 5%.

These results highlight that this robust design is able to tackle different competing trade-off objectives at the same time and provides a balanced solution for a better global performance. Recall that this is achieved by only optimizing the rigid-body controller gains (the bending filters are kept the same as the baseline). In this regard, this shows there is still room for further improvement when also considering the bending filters' design in an integrated design optimization framework.

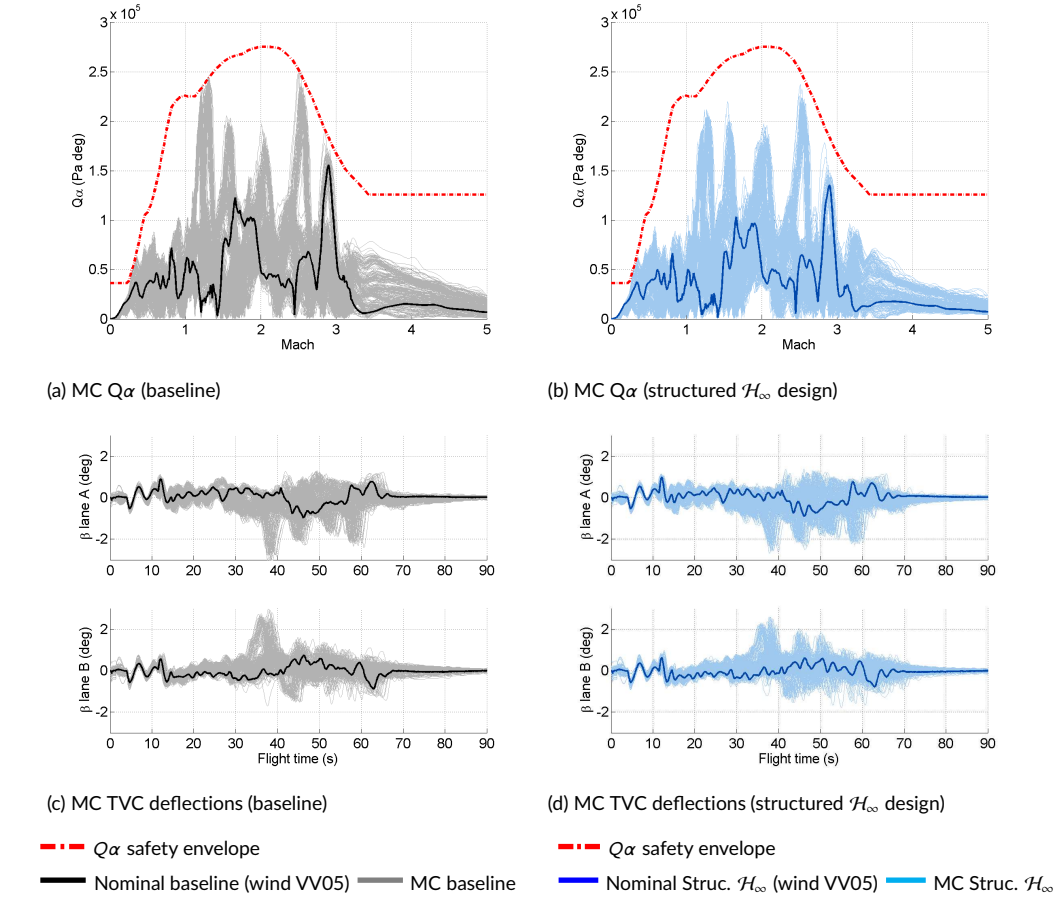

(a) MC Qα (baseline)

(b) MC Qα (structured $\mathcal{H}_\infty$ design)

(c) MC TVC deflections (baseline)

(d) MC TVC deflections (structured $\mathcal{H}_\infty$ design)

FIGURE 19 VEGACONTROL Monte Carlo responses

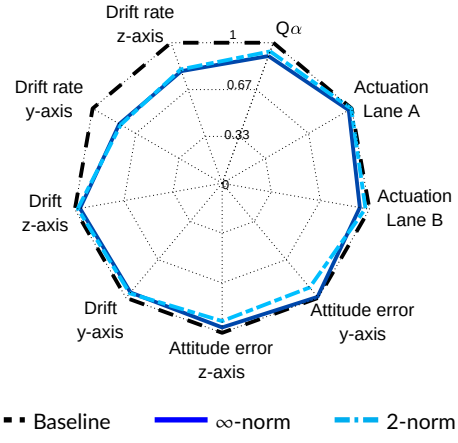

FIGURE 20 MC quantitative assessment

5 | CONCLUSION

This article describes a systematic robust control synthesis framework for the atmospheric control system design of a launch vehicle. In this work, the structured $\mathcal{H}_\infty$ technique is applied to the actual VEGA VV05 mission data for the design of the rigid-body controller. The main aim is to highlight the design and analysis capabilities of a more methodological framework with respect to the classical methods.

Firstly, with the objective of building industrial confidence in this synthesis framework, it is shown that the structured $\mathcal{H}_\infty$ control problem can be formulated to recover the classically designed VEGA VV05 mission rigid-body baseline controller, but in a more methodological manner. This legacy recovery exercise is based on a good understanding of the constraints introduced by the controller structure into the system. This is especially important since it facilitates the weighting function selection process.

In order to explore the potential for improvement over the traditional state-of-practice, the design interconnection is augmented by including a wind turbulence Dryden filter and subsequently also uncertain LFT models. The former provides the control optimiser with information about the wind levels and the frequency content of the wind disturbance. In this regard, it is highlighted that the use of strong wind levels for design contributes to improve the wind disturbance rejection performance for this mission. Moreover, the latter augmentation allows to perform the design against the expected variations of the system parameters.

Using this augmented configuration, the linear structured $\mathcal{H}_\infty$ controllers are synthesized and then analysed in terms of the traditional verification and validation process based on stability margins and nonlinear MC simulations. The system has also been analysed using the structured singular value μ, which provides analytically guaranteed bounds on robust stability. This analysis tool provides a direct connection to design, since it gives a good insight on the robustness of the system without applying an extensive MC validation process.

The final, scheduled (augmented structured $\mathcal{H}_\infty$) controller design provides robust stability throughout the flight envelope and improved robust performance with respect to the baseline controller. These results highlight the room for improvement that can be achieved by increasing the information provided to the control optimisation. In addition, they also show the capability of the synthesis framework to tackle the direct trade-off of robustness versus performance using a more comprehensive methodology.

acknowledgements

This work is funded by the European Space Agency (ESA) through the Networking/Partnering Initiative contract No. 4000114460/15/NL/MH/ats. Mr. Navarro-Tapia is also the recipient of a Doctoral Training Partnership award No. 1609551 by the UK Engineering and Physical Sciences Research Council (EPSRC).

references

[1] Roux C, Cruciani I. Scheduling schemes and control law robustness in atmospheric flight of VEGA launcher. In: Proceedings of the 7^{th} ESA International Conference on Spacecraft Guidance, Navigation and Control Systems; 2008. .

[2] Apkarian P, Noll D. Nonsmooth $\mathcal{H}_\infty$ synthesis. IEEE Transactions on Automatic Control 2006;51(1):71–86.

[3] Apkarian P, Dao MN, Noll D. Parametric Robust Structured Control Design. IEEE Transactions on Automatic Control 2015;60(7):1857–1869.

[4] Falcoz A, Pittet C, Bennani S, Guignard A, Bayart C, Frapard B. Systematic Design Methods of Robust and Structured Controllers for Satellites. CEAS Space Journal 2015;7(3):319–334.

[5] Pittet C, Prieur P. In: Structured Accelero-Stellar Estimator for Microscope Drag-Free Mission Springer International Publishing; 2015. p. 591–604.

[6] Marcos A, Sato M. Flight Testing of an Structured $\mathcal{H}_\infty$ Controller: an EU-Japan Collaborative Experience. In: Proceedings of the 1^{st} IEEE Conference on Control Technology and Applications; 2017. p. 1590–1595.

[7] Saussié D, Barbès Q, Bérard C. Self-scheduled and structured $\mathcal{H}_\infty$ synthesis : a launch vehicle application. In: Proceedings of the American Control Conference; 2013. p. 1590–1595.

[8] Knoblauch M, Saussié D, Bérard C. Structured H_∞ control for a launch vehicle. In: Proceedings of the American Control Conference; 2012. p. 967–972.

[9] Ganet-Schoeller M. Towards structured $\mathcal{H}_\infty$ synthesis for flexible launcher. In: Proceedings of the 3^{rd} CEAS Conference on Guidance, Navigation and Control; 2015. .

[10] Ganet-Schoeller M, Desmariaux J, Combier C. Structured Control for Future European Launchers. AerospaceLab Journal 2017 September;(13):1–10.

[11] Simplício P, Bennani S, Marcos A, Roux C, Lefort X. Structured Singular-Value Analysis of the VEGA Launcher in Atmospheric Flight. Journal of Guidance, Control, and Dynamics 2016;39(6):1342–1355.

[12] Greensite AL. Analysis and Design of Space Vehicle Flight Control Systems. Volume I - Short Period Dynamics. NASA Contractor Report CR-820; 1967.

[13] Roux C, Cruciani I. Roll coupling effects on the stability margins for VEGA launcher. In: Proceedings of the AIAA Atmospheric Flight Mechanics Conference and Exhibit; 2007. .

[14] Orr J, Johnson M, Wetherbee J, McDuffie J. State Space Implementation of Linear Perturbation Dynamics Equations for Flexible Launch Vehicles. In: Proceedings of the AIAA Guidance, Navigation, and Control Conference; 2009. .

[15] Arianespace, VEGA Flight VV05; 2015. Http://www.arianespace.com/mission/vega-flight-vv05/.

[16] Navarro-Tapia D, Marcos A, Bennani S, Roux C. Structured $\mathcal{H}_\infty$ Control Based on Classical Control Parameters for the VEGA Launch Vehicle. In: Proceedings of the IEEE Conference on Control Applications; 2016. .

[17] Marcos A, Rosa P, Roux C, Bartolini M, Bennani S. An Overview of the RFCS Project V&V Framework: Optimization-based and Linear Tools for Worst-Case Search. CEAS Space Journal 2015;7(2):303–318.

[18] Marcos A, Bennani S, Roux C, Valli M. LPV Modeling and LFT Uncertainty Identification for Robust Analysis: application to the VEGA Launcher during Atmospheric Phase. In: Proceedings of the 1^{st} IFAC Workshop on Linear Parameter Varying Systems; 2015. .

[19] Balas GJ, Chiang R, Packard A, Safonov MG. Robust Control Toolbox. The MathWorks, Inc.; 2005.

[20] Navarro-Tapia D, Marcos A, Bennani S, Roux C. Structured H_∞ Control Design for the VEGA Launch Vehicle: Recovery of the Legacy Control Behaviour. In: Proceedings of the 10^{th} International ESA Conference on Guidance, Navigation and Control Systems; 2017. .

[21] Navarro-Tapia D, Marcos A, Bennani S, Roux C. Structured $\mathcal{H}_\infty$ and Linear Parameter Varying Control Design for the VEGA Launch Vehicle. In: Proceedings of the 7^{th} European Conference for Aeronautics and Aerospace Sciences; 2017. .

[22] Gahinet P, Apkarian P. Structured $\mathcal{H}_\infty$ synthesis in MATLAB. In: Proceedings of the 18^{th} World Congress of the International Federation of Automatic Control, vol. 18; 2011. p. 1435–1440.

[23] Skogestad S, Postlethwaite I. Multivariable Feedback Control: Analysis and Design. John Wiley & Sons; 2005.

[24] Navarro-Tapia D, Marcos A, Bennani S, Roux C. Joint Robust Structured $\mathcal{H}_\infty$ Design of VEGA Launcher's Rigid-body Controller and Bending Filter. In: Proceedings of the 69^{th} International Astronautical Congress (IAC); 2018. .

[25] Geissler ED, McDonough GF, Murphree WD, Blair JC, Scoggins JR, Reed TG, et al. Wind Effects on Launch Vehicles. Technivision Services; 1970.

[26] Suzuki H. Load Relief Control of H-IIA Launch Vehicle. In: Proceedings of the 16^{th} IFAC Symposium on Automatic Control in Aerospace; 2004. p. 985–990.

[27] Hoelker RF. Theory of Artificial Stabilization of Missiles and Space Vehicles with Exposition of Four Control Principles. NASA Technical Note, NASA TN D-555; 1961.

[28] Harris RJ. Trajectory Simulation Applicable to Stability and Control Studies of Large Multi-Engine Vehicles. NASA Technical Note, NASA TN D-1838; 1963.

[29] Rheinfurth MH. Trajectory Simulation Applicable to Stability and Control Studies of Large Multi-Engine Vehicles. NASA Technical Memorandum, NASA TM X-53397; 1966.

[30] Johnson DL. Terrestrial Environment (Climatic) Criteria Guidelines for Use in Aerospace Vehicle Development. NASA Technical Memorandum, NASA TM 4511; 1993.